Testing of the GROMOS Force-Field Parameter Set 54A8: Structural Properties of Electrolyte Solutions, Lipid Bilayers, and Proteins

Maria M. Reif,[†] Moritz Winger,[‡] and Chris Oostenbrink*,[†]

[†]Institute for Molecular Modeling and Simulation, University of Natural Resources and Life Sciences, 1190 Vienna, Austria
[‡]Institute for Glycomics, Griffith University, Southport Qld 4222, Australia

S Supporting Information

ABSTRACT: The GROMOS 54A8 force field [Reif et al. *J. Chem. Theory Comput.* **2012**, *8*, 3705−3723] is the first of its kind to contain nonbonded parameters for charged amino acid side chains that are derived in a rigorously thermodynamic fashion, namely a calibration against single-ion hydration free energies. Considering charged moieties in solution, the most decisive signature of the GROMOS 54A8 force field in comparison to its predecessor 54A7 can probably be found in the thermodynamic equilibrium between salt-bridged ion pair formation and hydration. Possible shifts in this equilibrium might crucially affect the properties of electrolyte solutions or/and the stability of (bio)molecules. It is therefore important to investigate the consequences of the altered description of charged oligoatomic species in the GROMOS 54A8 force field. The present study focuses on examining the ability of the GROMOS 54A8 force field to accurately model the structural properties of electrolyte solutions, lipid bilayers, and proteins. It is found that (*i*) aqueous electrolytes involving oligoatomic species (sodium acetate, methylammonium chloride, guanidinium chloride) reproduce experimental salt activity derivatives for concentrations up to 1.0 m (1.0-molal) very well, and good agreement between simulated and experimental data is also reached for sodium acetate and methylammonium chloride at 2.0 m concentration, while not even qualitative agreement is found for sodium chloride throughout the whole range of examined concentrations, indicating a failure of the GROMOS 54A7 and 54A8 force-field parameter sets to correctly account for the balance between ion−ion and ion−water binding propensities of sodium and chloride ions; (*ii*) the GROMOS 54A8 force field reproduces the liquid crystalline-like phase of a hydrated DPPC bilayer at a pressure of 1 bar and a temperature of 323 K, the area per lipid being in agreement with experimental data, whereas other structural properties (volume per lipid, bilayer thickness) appear underestimated; (*iii*) the secondary structure of a range of different proteins simulated with the GROMOS 54A8 force field at pH 7 is maintained and compatible with experimental NMR data, while, as also observed for the GROMOS 54A7 force field, α-helices are slightly overstabilized with respect to 3_{10}-helices; (*iv*) with the GROMOS 54A8 force field, the side chains of arginine, lysine, aspartate, and glutamate residues appear slightly more hydrated and present a slight excess of oppositely-charged solution components in their vicinity, whereas salt-bridge formation properties between charged residues at the protein surface, as assessed by probability distributions of interionic distances, are largely equivalent in the GROMOS 54A7 and 54A8 force-field parameter sets.
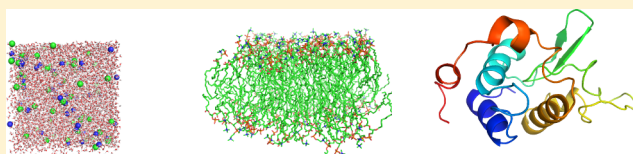
I. INTRODUCTION

(Bio)molecular systems at nonzero temperature are nowadays routinely described as ensembles of structures statistically representative of the phase space sampled by the system under given thermodynamic boundary conditions.[1−3] If the (bio)-molecular system of interest is considered at room temperature and in the condensed phase, quantum effects are usually negligible, and the sampling of configurations is thus required to satisfy the Boltzmann distribution. The generation of corresponding configurations can be performed numerically, e.g., based on a molecular dynamics (MD) integration scheme. In classical atomistic MD simulation, the atoms forming the molecular system are represented as mass-possessing point particles associated with a unique interaction site, and an empirical classical potential-energy function (force field) is used to derive the forces acting on the atoms.[4−6] The results obtained from MD simulations depend on the extent of sampling of the phase space accessible to the molecular system

and the accuracy of the underlying force field. A major effort in the reign of molecular simulation is thus directed toward the parametrization and validation of force fields against available experimental data.

A coarse distinction of available force fields can be made based on the purpose of the force field, which determines the underlying parametrization strategy. Spectroscopic force fields[7−13] are designed to investigate gas-phase molecular properties, and their parametrization aims at the accurate representation of molecular geometric, energetic, and vibrational properties, while thermodynamic force fields[14−22] are designed to investigate condensed-phase properties, the parametrization accordingly aiming at the accurate representation of bulk thermodynamic properties such as, e.g., densities, vaporization enthalpies, or solvation free energies. The present

study is concerned with the GROMOS force field for (bio)molecular simulation. For a thorough discussion of its history and philosophy, the reader is referred to ref 20. The most recent version of the GROMOS force field is the 54A8 parameter set,[22] which is based on (*i*) the simple-point-charges (SPC) water model;[23] (*ii*) neutral amino acid side chain parameters from the 53A6 force field,[24] obtained from optimization against pure-liquid properties and solvation free energies of small molecules; (*iii*) charged amino side chain parameters obtained from optimization against single-ion hydration free energies based on a standard absolute intrinsic proton hydration free energy of[25] $\Delta G_{hyd}^{\ominus}[H_g^+]$ = −1100 kJ·mol^{-1}; (*iv*) carbohydrate parameters from the 45A4 force field, along with atomic partial charges from ref 26 obtained from restrained electrostatic potential (RESP) fitting compatible with the 53A6 force field; (*v*) nucleic-acid parameters from the 45A4 force field, along with dihedral angles obtained from quantum-mechanical calculations and atomic partial charges compatible with the 53A6 force field, by ref 27; (*vi*) lipid parameters from ref 28, along with atomic partial charges from ref 29; (*vii*) sodium and chloride ion parameters from ref 30 obtained from optimization against single-ion hydration free energies based on a standard absolute intrinsic proton hydration free energy of[25] $\Delta G_{hyd}^{\ominus}[H_g^+]$ = −1100 kJ·mol^{-1}. Besides, alternative parameter sets compatible with the GROMOS force field are available, as e.g. for saturated and unsaturated lipid molecules with phosphocholine or phosphoglycerol head groups,[31] and for hexapyranose-based carbohydrate molecules.[32−34]

Three putative shortcomings of the GROMOS 54A8 force-field parameter set require careful investigation:

1. A crucial feature of the GROMOS 54A8 force-field parametrization strategy is the usage of methodology-independent ion hydration free energies, i.e. the molecular ions analogous to charged amino acid side chain functionalities (guanidinium for arginine, imidazolium for histidine, methyl-ammonium for lysine, and acetate for aspartate and glutamate) were calibrated for the ideal situation of Coulombic electrostatic interactions in a macroscopic nonperiodic system. However, currently, limitations in computing power prohibit the conduction of simulations according to this ideal situation. Typically, systems of finite size and approximate electrostatic interaction functions are resorted to, and the resulting discrepancy between the representation of the charged functional groups during the parametrization procedure (post-simulation correction of raw hydration free energies obtained from configurations sampled with spurious forces for approximate electrostatics, finite-size, and potential-summation artifacts) and during configurational sampling in actual (bio)molecular simulations (no correction for approximate electrostatics, finite-size, and potential-summation artifacts at the level of forces) might lead to artifacts in the configurational sampling. For instance, since the correction terms coining methodology-independent ion hydration free energies are predominantly negative, ions might in effect be underhydrated during simulations, this effect being more pronounced for cations than for anions and presumptively also more pronounced for monatomic ions (concentrated charge density) compared to oligoatomic ones (more diffuse charge density),[22] and a possible consequence of the decreased effective hydrophilicity of charged functional groups might manifest in an overestimation of ion–ion binding in solution, or an

underestimation of the interaction of protein side chains with the solvent.

2. Not all charged functional groups were reparameterized in the development of the GROMOS 54A8 force-field parameter set. For instance, the phosphate ion has unaltered Lennard-Jones parameters and atomic partial charges which might not yield a hydration free energy compatible with the above choice of proton hydration free energy and consequently imply imbalances in the relative interaction energies of this ion with other charged functional groups and with water as a solvent.

3. The GROMOS force field relies on a geometric-mean combination rule[35] to define heteroatomic Lennard-Jones interaction parameters based on homoatomic ones. Although a physical rationalization of this rule based on atomic polarizability products in the Slater–Kirkwood formula for dispersion coefficients[36] may be conceived of in the case of interactions between isolated monatomic species, it remains truly *ad hoc* for repulsion coefficients and in the case of interactions between atoms in molecules, and one is hence bound to question its tenability upon translation of Lennard-Jones interaction parameters valid in a system governed by few heteroatomic interactions (e.g., a single acetate ion in aqueous solution) to an environment characterized by multiple interactions with molecular species and functional groups other than water [e.g., an acetate ion in a 1.0 m (1.0-molal) aqueous sodium acetate solution, or a carboxylate group pertaining to a glutamate residue in a protein].

In the context of (bio)molecular simulation, it has therefore to be tested whether, e.g., biomacromolecular structure and dynamics, the structural, dynamic, and thermodynamic properties of electrolyte solutions, and interactions between the two latter types of systems as, e.g., encountered in the province of Hofmeister effects[37−40] on biomacromolecules, are accounted for in a realistic way. Considering aqueous electrolyte solutions involving ionic species parametrized against methodology-independent hydration free energies, a realistic description of the thermodynamic equilibrium between ion–ion and ion–water pairing propensities in the GROMOS 54A8 force field is not *a priori* guaranteed because (*i*) interionic distances and water configurations sampled in systems of finite sizes and with approximate electrostatic interaction functions might lead to artificial interionic distance distributions and inadequate ion hydration[41] and (*ii*) the geometric-mean combination rule applied on the basis of optimal ion–water Lennard-Jones interactions might prove inadequate for the representation of ion–ion Lennard-Jones interactions.[42]

Considering arrangements of lipid molecules in solution, the increased van der Waals radius of the methyl group attached to positively charged species is expected to be reflected in structural parameters such as, e.g., area per lipid of choline-headgroup containing lipids. In the GROMOS 54A7 force field,[21] the repulsion between choline methyl groups and phosphate oxygen atoms was increased to reproduce experimental properties for the liquid crystalline-like phase.[28] In the GROMOS 54A8 force field, this change was reverted, because the increased Lennard-Jones repulsion parameter of the choline methyl group in comparison to the GROMOS 54A7 force field achieves approximately the same alteration in lipid headgroup repulsion (section III.2).[22]

Considering native proteins in solution, the most decisive signature of the GROMOS 54A8 force field in comparison to its predecessor 54A7 can probably be found in the thermodynamic equilibrium between salt-bridge formation

Table 1. Abbreviations for the Simulated Systems and Performed Simulations Used Throughout the Text[a]

abbreviation	system and simulation specification	force field	simulation time [ns]	$\langle L \rangle$ [nm]
	electrolyte solutions			
NA-CL	0.5, 1.0, or 2.0 m aqueous sodium chloride solution	54A8	6	5.98,[b] 5.95,[c] 5.93[d]
NA-ACET	0.5, 1.0, or 2.0 m aqueous sodium acetate solution	54A8	6	6.00,[b] 5.98,[c] 5.98[d]
H3C1-CL	0.5, 1.0, or 2.0 m aqueous methylammonium chloride solution	54A8	6	6.02,[b] 6.03,[c] 6.07[d]
GUAN-CL	0.5, 1.0, or 2.0 m aqueous guanidinium chloride solution	54A8	6	6.03,[b] 6.04,[c] 6.10[d]
	lipid bilayers			
$DPPC_1$	hydrated DPPC bilayer	54A8	40	6.41,[e] 8.29[f]
$DPPC_2$	hydrated DPPC bilayer	g	40	6.62,[e] 7.79[f]
$DPPC_3$	hydrated DPPC bilayer	h	40	6.73,[e] 7.53[f]
	proteins			
HEWL	hen egg white lysozyme in water	54A8	20	7.72
FOX	RNA-binding domain of the human FOX-1 protein in complex with a UGCAUGU RNA strand in water	54A8	20	7.18
CM	chorismate mutase of *Mycobacterium tuberculosis* in water	54A8	20	8.86
GCN	GCN4 trigger peptide in water	54A8	100	4.48
PROTG	B1 immunoglobulin-binding domain of streptococcal protein G in water	54A8	20	6.19
COLDS	major cold chock protein CspA of *Escherichia coli* in water	54A8	20	6.38
SAC_0^{54A7}	hyperthermophilic protein Sac7d of *Sulfolobus acidocaldarius* (SAC) in water	54A7	20	6.60
SAC_0^{54A8}	SAC in water	54A8	20	6.60
$SAC_{Cl^-}^{54A7}$	SAC in water, with six chloride counterions	54A7	20	6.60
$SAC_{Cl^-}^{54A8}$	SAC in water, with six chloride counterions	54A8	20	6.60
SAC_{NaCl}^{54A7}	SAC in water, with six sodium and 12 chloride counterions	54A7	20	6.60
SAC_{NaCl}^{54A8}	SAC in water, with six sodium and 12 chloride counterions	54A8	20	6.60

[a]The indicated simulation time refers to the length of the production run, and the reported box-edge lengths $\langle L \rangle$ are arithmetic averages over the production run. If not indicated otherwise, a neutralizing amount of sodium or chloride counterions was used in the protein simulations. More details are provided in sections II.1.1, II.1.2, and II.1.3 for simulations involving electrolyte solutions, lipid bilayers, and proteins, respectively. [b]0.5 m. [c]1.0 m. [d]2.0 m. [e]Box-edge length along the bilayer plane. [f]Box-edge length along the bilayer normal. [g]Modified GROMOS 54A8 force-field parameter set, where the $C_{12}^{ii,(2)}$ parameter of atom type 2 is employed for interactions with atom type 54. [h]Modified GROMOS 54A8 force-field parameter set, where the $C_{12}^{ii,(3)}$ parameter of atom type 2 is employed for interactions with atom type 54.

Table 2. Computed and Experimental Activity Derivatives f_{ss} (eq 2) for the Salts NA-CL, NA-ACET, H3C1-CL, and GUAN-CL Corresponding to Aqueous Electrolyte Solutions of Salt Molality b_s[a]

	b_s [m]	x_s	N_s	N_w	G_{ss} [nm³]	G_{sw} [nm³]	G_{ww} [nm³]	$\langle L^3 \rangle$ [nm³]	f_{ss} (sim.)	f_{ss} (exp.)
NA-CL	0.5	0.0177	62	6881	0.64	−0.013	−0.029	214.0	−0.27	−0.055
NA-ACET					−0.11	−0.025	−0.029	215.7	0.05	0.017
H3C1-CL					0.011	−0.044	−0.028	218.5	−0.04	−0.106
GUAN-CL					0.21	−0.060	−0.028	219.5	−0.14	−0.194
NA-CL	1.0	0.0348	121	6715	0.66	−0.026	−0.029	210.3	−0.43	0.011
NA-ACET					−0.11	−0.023	−0.029	213.5	0.11	0.135
H3C1-CL					−0.038	−0.043	−0.028	218.9	−0.02	−0.063
GUAN-CL					0.12	−0.063	−0.027	220.8	−0.19	−0.246
NA-CL	2.0	0.0672	235	6521	1.69	−0.092	−0.026	208.1	−0.80	0.169
NA-ACET					−0.12	−0.020	−0.029	213.7	0.29	0.354
H3C1-CL					−0.090	−0.038	−0.028	224.0	0.09	0.046
GUAN-CL					−0.008	−0.062	−0.024	227.5	−0.15	−0.302

[a]The reported data include the number of cations N_s, the number of anions N_s, the number of water molecules N_w, the corresponding salt mole fraction x_s (eq A.3), the average volume of the computational box $\langle L^3 \rangle$, as well as the Kirkwood−Buff integrals G_{IJ} for salt−salt (ss), salt−water (sw), and water−water (ww) interactions. The experimental activity derivatives are obtained from the fitted functions given by eq A.2 using the coefficients a, b, c, and d reported in the Supporting Information, Table SI. Simulated activity derivatives are calculated according to eq 5, using Kirkwood−Buff integrals G_{IJ} given by the y-axis intercept of a linear fit to $G_{IJ}(L_s^{-1})$, as displayed in Figure 1.

and hydration of charged functional groups at the protein surface. Since salt bridges influence protein stability only marginally,[43−46] it can be expected that the GROMOS 54A8 force field yields stable proteins akin to the GROMOS 54A7 force field. Similar considerations apply to the situation of proteins in aqueous electrolyte solutions. On the basis of the law of "matching water affinities",[40,47,48] it may be presumed that weakly hydrated anionic species (e.g., chloride ions) bind

directly to positively charged functional groups in a protein (which are likewise weakly hydrated) and that strongly hydrated cationic species (e.g., sodium ions) bind directly to protein carboxylate groups (which are likewise strongly hydrated). However, failure to properly account for the underlying free energies of hydration may confound the relative ion pairing propensities, which could entail an erroneous classification of ions concerning their effect on

protein stability ("Hofmeister series,"[38] e.g. salting-in vs salting-out phenomena).

The goal of this article is to investigate some of the above issues in simulations of electrolyte solutions, lipid bilayers, and proteins. In particular, it is studied whether (*i*) thermodynamic properties (experimental activity derivatives) of electrolyte solutions are correctly reproduced; (*ii*) usage of the GROMOS 54A8 force-field representation of the tetramethylammonium ion[22] in the positively charged choline headgroup of phosphatidylcholine lipids still achieves a realistic description of lipid bilayer structural properties; (*iii*) the GROMOS 54A8 force field yields stable protein secondary structures compatible with experimental NMR data (NOE values and ^3J-coupling constants; where available); (*iv*) protein surface salt-bridge formation and counterion binding properties differ between the GROMOS 54A7 and 54A8 force fields. The results of these investigations are expected to be sensitive to the employed simulation methodology. In order for them to be of highest relevance to the GROMOS user community, the most widely used simulation protocol is employed,[49] which implies, notably, a cutoff-truncated electrostatic interaction function with reaction-field correction. However, in the case of simulations of electrolyte solutions, an exception to the standard protocol is made, and a lattice-sum electrostatic interaction function is used. This was necessary to allow a valid comparison with experimental data for those highly electrostatic artifact-prone systems.

II. COMPUTATIONAL DETAILS

II.1. Setup of Simulated Systems. The simulated systems and performed simulations are summarized in Table 1.

II.1.1. Electrolyte Solutions. Aqueous 0.5, 1.0, and 2.0 m solutions of sodium chloride (NA-CL), sodium acetate (NA-ACET), methylammonium chloride (H3C1-CL), and guanidinium chloride (GUAN-CL) were created by randomly placing N_s ion pairs and N_w water molecules (Table 2), the latter represented by the SPC water model,[23] in cubic computational boxes whose sizes were as a first approximation chosen such that the overall molecule number density satisfied the equilibrated number density of the SPC water model (32.5 nm^{-3}).[50] An equilibration run consisting of 4 ns with cutoff-truncated electrostatic interactions including a Barker–Watts reaction-field correction and 1 ns with LS electrostatic interactions was performed in the NPT ensemble at a pressure of 1 bar and a temperature of 298.15 K. Further details concerning the handling of electrostatic interactions are provided in section II.2.

II.1.2. Lipid Bilayers. A configuration of a hydrated dipalmitoylphosphatidylcholine (DPPC) bilayer obtained after 190 ns of MD simulation with the GROMOS 54A7 force field at a pressure of 1 bar and a temperature of 323 K by ref 28 was downloaded from the automated topology builder repository.[51] It contains 128 DPPC molecules (8×8 molecules per leaflet) in the liquid crystalline-like phase and 5841 SPC water molecules in a box of dimensions $6.3398 \times 6.3398 \times 8.3985$ nm^3, the bilayer plane being parallel to the xy plane of the computational box. The area per lipid A_L (eq 7) of this configuration thus evaluates to 0.628 nm^2, close to the experimental values reported by ref 52 (0.629 nm^2) and ref 53 (0.630 nm^2) and somewhat lower than the values reported by ref 54 (0.64 nm^2) and ref 55 (0.642–0.643 nm^2). This configuration was used as the starting configuration in three MD simulations denoted DPPC$_1$, DPPC$_2$, and DPPC$_3$, which

differ in the C_{12}^{ii} parameter of the phosphate oxygen atom type (atom type 2 in the GROMOS 54A7 and 54A8 force fields) to be used for interactions with the methyl group in the choline headgroup (atom type 54 in the GROMOS 54A7 and 54A8 force fields), namely $[C_{12}^{ii,(1)}]^{1/2} = 0.8611 \times 10^{-3}$, $[C_{12}^{ii,(2)}]^{1/2} = 1.841 \times 10^{-3}$, or $[C_{12}^{ii,(3)}]^{1/2} = 3.068 \times 10^{-3}$ kJ$^{1/2}$·mol$^{-1/2}$·nm^6, respectively. The first choice was adopted in the construction of the GROMOS 54A8 force field, i.e., simulation DPPC$_1$ corresponds to this set of force-field parameters (section I), whereas simulations DPPC$_2$ and DPPC$_3$ present increased Lennard-Jones repulsion between the choline head groups and the phosphate oxygen atoms. The third choice (albeit in combination with a C_{12}^{ii} parameter of atom type 54 that is lower than in the GROMOS 54A8 force field) was adopted in the construction of the GROMOS 54A7 force field.[21,28] Note, in addition, that unlike previous GROMOS force-field parameter sets, the GROMOS 54A7 and 54A8 force-field representations of the DPPC molecule adopt the atom partial charge distribution of Chiu et al.[29] These charges are derived from *ab initio* quantum-mechanical calculations and turn out to be significantly enhanced in magnitude in comparison to their GROMOS pre-54A7 analogs. Although adherence to quantum-mechanically derived charge distributions is actually at variance with the philosophy of the GROMOS force field,[3,35] it turned out necessary in this specific case to adequately model the biologically important liquid crystalline-like phase of DPPC bilayers.[28]

The structure downloaded from the automated topology builder repository[51] corresponds to a temperature of 323 K, but as no velocities were available it was equilibrated in six successive MD runs each of 20 ps length in the NVT ensemble, for each of the DPPC$_1$, DPPC$_2$, and DPPC$_3$ simulations. The three simulations were initiated from a random set of atom velocities satisfying a Maxwell–Boltzmann distribution at 60 K. In the first simulation period, harmonic position restraints on the lipid atoms were applied with a force constant of 2.5×10^4 kJ·mol^{-1}·nm^{-2}. In the subsequent simulations, the temperature was increased to 120, 180, 240, 300, and 323 K while the force constant was reduced to 2.5×10^3, 2.5×10^2, 25, 2.5, and 0 kJ·mol^{-1}·nm^{-2}, respectively.

II.1.3. Proteins. Hen egg white lysozyme (HEWL), the RNA-binding domain of the human FOX-1 protein in complex with a UGCAUGU RNA strand (FOX), chorismate mutase of *Mycobacterium tuberculosis* (CM), the GCN4 trigger peptide (GCN), the B1 immunoglobulin-binding domain of streptococcal protein G (PROTG), the major cold chock protein CspA of *Escherichia coli* (COLDS), and the hyperthermophilic protein Sac7d of *Sulfolobus acidocaldarius* (SAC) were simulated with the GROMOS 54A8 force field to investigate secondary structure stability and, where available, compatibility of simulation results with experimental NMR data. SAC was in addition simulated with the GROMOS 54A7 force field because it contains a multitude of charged surface residues. For this protein, a comparison between both force fields in terms of surface salt-bridge formation and counterion binding properties thus appears interesting.

Starting configurations for HEWL, FOX, CM and GCN were provided by the authors of ref 21 who used these systems for testing the GROMOS 54A7 force field, i.e., these starting configurations are rigorously identical to those used in ref 21 and correspond to entries 1AKI (HEWL; X-ray diffraction structure at 1.5 Å resolution),[56] 2ERR (FOX; entry number 1 from a solution-NMR structure bundle),[57] 2FP2 (CM; X-ray

diffraction structure at 1.6 Å resolution),[58] and 2OVN (GCN; entry number 1 from a solution-NMR structure bundle)[59] in the Protein Data Bank (PDB). Starting configurations for COLDS and PROTG were provided by a collaborator in GROMOS force-field development (Andreas P. Eichenberger, personal communication) and correspond to PDB entries 1MJC (COLDS; X-ray diffraction structure at 2.0 Å resolution)[60] and 1PGB (PROTG; X-ray diffraction structure at 1.9 Å resolution).[61] Finally, a starting configuration for SAC was derived from PDB entry 1SAP (solution-NMR structure).[62] This PDB entry does not provide experimental Nuclear Overhauser Enhancement (NOE) values for SAC. In the following, the details of the system preparation protocol for 1SAP are provided and are, for the sake of completeness, also briefly repeated for the other proteins.

The X-ray diffraction structures (in the case of CM, only the first subunit of the reported dimer) and the first structures of the NMR bundles (FOX, GCN) were complemented with missing hydrogen coordinates if necessary, relaxed in a vacuum using the steepest-descent energy minimization functionality of the GROMOS11 program,[49] and solvated in cubic computational boxes composed of periodically replicated cubic water boxes containing 216 SPC water molecules at the equilibrated density of the SPC water model (972 kg·m^{-3}),[50] allowing for a minimum protein−solvent distance of 0.23 nm. The resulting box-edge lengths are reported in Table 1. To remove steric strain involving the solvent molecules, another steepest-descent energy minimization was applied. During this procedure, the solute atom positions were restrained to their initial positions using a force constant 2.5×10^4 kJ·mol^{-1}·nm^{-2}. In simulations HEWL, CM, PROTG, and COLDS, a neutralizing amount of sodium or chloride counterions was added by replacing randomly chosen water molecules within the bulk solvent. In simulations FOX and GCN, no counterions were added to maintain consistency with previous studies involving these proteins.[21,63] All simulations were performed with amino acid side chain and terminal-group protonation states appropriate for pH 7, i.e., all arginine, lysine, aspartate, and glutamate residues, as well as protein termini were charged. One exception is formed by residue K5 of the FOX protein, which was kept deprotonated to maintain consistency with previous studies involving this protein[21,63] where the deprotonation of this residue was erroneously introduced. The resulting number of charged side chains is reported in Table 4, and it follows that simulations HEWL, FOX, CM, GCN, PROTG, and COLDS involve net charges of 0, −4, 0, +1, 0, and 0e, respectively, where the charge of −6e of the RNA molecule binding to the FOX protein was taken into account. For SAC, the system preparation followed the same protocol, except for the following: (*i*) systems were prepared for both GROMOS 54A7 and 54A8 force fields (corresponding simulations are denoted with superscripts "54A7" and "54A8"; Table 1); (*ii*) the protein was not minimized *in vacuo* to avoid possible structural disruptions which might arise as a consequence of spurious salt-bridge formation between the many charged surface residues. Instead, a steepest-descent energy minimization was done for the entire system after solvation; (*iii*) addition of counterions was not only done with the aim of neutralizing the protein, which carries a net charge of +6e. Instead, for each force-field parameter set, three approaches were investigated, namely omission of counterions (denoted SAC$_0$), addition of a neutralizing amount of chloride ions (denoted SAC$_{Cl^-}$), or addition of a neutralizing sodium chloride

solution consisting of 12 chloride and six sodium ions (denoted SAC$_{NaCl}$).

All simulations were initiated from a random set of atom velocities satisfying a Maxwell−Boltzmann distribution at 60 K, and the systems were equilibrated in five successive MD runs each of 20 ps length in the NVT ensemble. In the first simulation period, harmonic position restraints on the protein atoms were applied with a force constant of 2.5×10^4 kJ·mol^{-1}·nm^{-2}. In the subsequent simulations, the temperature was increased to 120, 180, 240, and 300 K, while the force constant was reduced to 2.5×10^3, 2.5×10^2, 25, and 0 kJ·mol^{-1}·nm^{-2}, respectively. For CM, a temperature of 310 K was used in the fifth run to maintain consistency with a previous study[21] involving this protein.

II.2. Molecular Dynamics Simulations. Twelve simulations of electrolyte solutions, three simulations of hydrated lipid bilayers, and 12 simulations of hydrated proteins were performed using the GROMOS11 package of programs[49] (Table 1). Production runs were started from equilibrated system configurations obtained as described in section II.1. They lasted 6 ns for the electrolyte solutions, 40 ns for the lipid bilayers, 20 ns for all protein systems except GCN, and 100 ns for GCN. See Supporting Information section S.I for details on the simulation settings.[35,64−78]

II.3. Analysis of Simulation Results. *II.3.1. Calculation of Electrolyte Activity Derivatives.* The rational (mole-fraction scale) activity coefficient f_s of a salt relates the salt activity a_s to the salt mole fraction x_s, i.e.[79]

$$a_s = f_s x_s \tag{1}$$

The activity derivative f_{ss} is given by

$$f_{ss} = \left(\frac{\partial \ln f_s}{\partial \ln x_s} \right)_{P,T} \tag{2}$$

and can be evaluated from the structural characteristics of the electrolyte solution by means of a Kirkwood−Buff analysis, because Kirkwood−Buff theory[80−82] establishes the necessary connection between thermodynamic and structural solution properties. The latter are characterized through Kirkwood−Buff integrals[80] G_{IJ}, which may be calculated on the basis of radial distribution functions (rdfs) $g_{IJ}^{\mu VT}(r)$ of particles I and J obtained from MD simulations in the μVT ensemble but are generally approximated using rdfs $g_{IJ}^{NPT}(r)$ corresponding to the NPT ensemble, i.e.

$$G_{IJ} = 4\pi \int_0^\infty dr [g_{IJ}^{\mu VT}(r) - 1] r^2$$
$$\approx 4\pi \int_0^\infty dr [g_{IJ}^{NPT}(r) - 1] r^2 \tag{3}$$

or on the basis of particle number fluctuations in the μVT ensemble, i.e.

$$G_{IJ} = V \frac{\langle N_I N_J \rangle - \langle N_I \rangle \langle N_J \rangle}{\langle N_I \rangle \langle N_J \rangle} - \delta_{IJ} V \langle N_I \rangle^{-1} \tag{4}$$

where N_I and N_J denote the number of particles I and J, respectively, angular brackets denote an ensemble average, and δ_{IJ} denotes the Dirac delta function ($\delta_{IJ} = 1$ for $I = J$ and zero otherwise).

For the approach based on eq 3, the integration is in practice performed from 0 to finite distances r smaller than half the edge length of the computational box, and the Kirkwood−Buff

integrals $G_{IJ}(r) = 4\pi \int_0^r dr' [g_{IJ}^{NPT}(r') - 1] r'^2$ are averaged over a range of values r for which the rdfs are reasonably close to the bulk value $g_{IJ}^{NPT}(\infty) = 1$. If $I = J$ and the rdfs are obtained from a simulation at constant particle number, a finite-size correction (typically *via* scaling of the rdf) has to be applied to account for the reduced like-particle density around the central particle.[48]

The approach based on eq 4 was suggested[83,84] to be performed in a sub-box of edge length L_s cut out from a larger box for which a simulation trajectory pertaining to a constant-particle-number ensemble is available. In this case, the volume V in eq 4 is to be replaced by the volume of the sub-box, L_s^3, and the particle numbers N_I and N_J in eq 4 are counted in the sub-box. Thus, N_I and N_J are not constant, i.e., effectively correspond to an open ensemble. Finite-size effects may be accounted for by evaluating eq 4 for multiple values of L_s and extrapolating the linear regime of $G_{IJ}(L_s^{-1})$ to $L_s^{-1} = 0$.[83,84] The authors of the present study experienced difficulties with the convergence of $G_{IJ}(r)$ calculated *via* eq 3 for salt−water and salt−salt interactions. Therefore, $G_{IJ}(L_s^{-1})$ was calculated *via* eq 4 for randomly positioned cubic sub-boxes of edge length L_s ranging from 0.5 to 1.0 nm in steps of 0.05 nm and from 1.0 to 5.25 nm in steps of 0.25 nm, and a finite-size corrected value G_{IJ} was obtained as the y-axis intercept of a linear fit to $G_{IJ}(L_s^{-1})$. Although small values of L_s allow analysis of multiple nonoverlapping sub-boxes per trajectory frame, this was not done in the present study because plain analysis using one sub-box per trajectory frame already provided sufficient statistics. The counting of oligoatomic ions and water molecules in the sub-box relied on the carboxylate carbon atoms of acetate ions, the nitrogen atoms of methylammonium ions, the carbon atoms of guanidinium ions, and the oxygen atoms of water molecules. For most of the salts and concentrations examined, the resulting Kirkwood−Buff integrals turned out to be similar to the values obtained with the rdf-based approach (eq 3) if the above-mentioned averaging of $G_{IJ}(r)$ was done over the interval $1.0 \leq r \leq 1.5$ nm (data not shown).

The activity derivative f_{ss} is related to the salt−salt (ss), salt−water (sw), and water−water (ww) Kirkwood−Buff integrals as[81]

$$f_{ss} = -\frac{x_s \eta_w \Delta G}{1 + x_s \eta_w \Delta G} \tag{5}$$

where η_w is the number of density of water molecules and

$$\Delta G = G_{ss} + G_{ww} - 2G_{sw} \tag{6}$$

Note that the above outline of the application of Kirkwood−Buff theory to an electrolyte solution treats cations and anions as indistinguishable particles.[85,86] This approach allows a meaningful comparison to experimental activity derivative data, the corresponding activity coefficients being, due to the electroneutrality of macroscopic matter at equilibrium, mean rather than single-ion values, i.e. $f_s^2 = f_{I_{aq}^z} f_{J_{aq}^{-z}}$ for a 1:1 electrolyte composed of ions I_{aq}^z and J_{aq}^{-z}.

Experimental data for f_{ss} can be obtained by differentiation of fitted functions for experimental f_s values (Appendix, eq A.7).

II.3.2. Biomolecular Structure. The structural properties of the simulated DPPC lipid bilayers were analyzed in terms of area and volume per lipid and electron density profiles. The average area per lipid A_L and volume per lipid V_L were calculated as

$$A_L = \frac{2\langle L_x L_y \rangle}{N_L} \tag{7}$$

and

$$V_L = \frac{\langle V_{BL} \rangle}{N_L} \tag{8}$$

respectively, where $N_L = 128$ is the number of DPPC molecules, $L_x L_y$ is the area of one lipid bilayer leaflet in the computational box, calculated as the product of the box-edge lengths along the x and y directions, and $V_{BL} = L_x L_y L_z - N_w V_{H2O}$ is the volume of the computational box occupied by the lipid bilayer, calculated as the box volume $L_x L_y L_z$ reduced by an estimate $N_w V_{H2O}$ for the volume of the box occupied by water. The latter is approximated as the product of the number of water molecules $N_w = 5841$ and an estimate for the volume of one SPC water molecule V_{H2O} under the given pressure and temperature conditions ($V_{H2O} = 3.15 \times 10^{-2}$ nm^3 at $P = 1$ bar and $T = 323$ K).[28] The electron density profile $\eta_e(z)$ along the bilayer normal direction was calculated as

$$\eta_e(z) = n_e(P)\langle N_P(z; z') \rangle + n_e(O)\langle N_O(z; z') \rangle$$
$$+ n_e(N)\langle N_N(z; z') \rangle + n_e(C)\langle N_C(z; z') \rangle \tag{9}$$

where z' denotes the signed distance of an atom from the bilayer center, $n_e(P) = 16$, $n_e(O) = 8$, $n_e(N) = 6$, and $n_e(C) = 6$ are the numbers of electrons of phosphorus, oxygen, nitrogen, and carbon atoms, respectively, and $\langle N_P(z;z') \rangle$, $\langle N_O(z;z') \rangle$, $\langle N_N(z;z') \rangle$, and $\langle N_C(z;z') \rangle$ are the average numbers of these atoms sampled at distances $|z| - (1/2)\Delta z \leq |z'| < |z| + (1/2)\Delta z$ from the bilayer center. Electron numbers of 16 and 6 for phosphorus and nitrogen, respectively, account for the net charge of the phosphate and choline groups, respectively. Electrons of hydrogen atoms associated with the united-atom methylene and methyl groups were neglected. z ranges from $-L_z/2 + \Delta z/2$ to $L_z/2 - \Delta z/2$, and the bin width Δz is $L_z/100$. The electron density profile of a lipid bilayer in the liquid crystalline-like phase presents two maxima whose positions are mostly determined by the electron-rich phosphorus atoms. The distance between maxima in the electron density of lipid headgroup atoms, $\eta_{e(H)}(z)$, is referred to as the head−head bilayer thickness D_{HH}.[28] Here, the headgroup atoms chosen for calculation of the electron density profile involve the choline and the phosphate group, i.e., three united-atom methyl groups, a nitrogen atom, two united-atom methylene groups, one phosphorus atom, and four oxygen atoms, such that

$$\eta_{e(H)}(z) = n_e(P)\langle N_P(z; z') \rangle + n_e(O)\langle N_{O \in H}(z; z') \rangle$$
$$+ n_e(N)\langle N_N(z; z') \rangle + n_e(C)\langle N_{C \in H}(z; z') \rangle \tag{10}$$

where $\langle N_{O \in H}(z;z') \rangle$ and $\langle N_{C \in H}(z;z') \rangle$ refer to oxygen and carbon atoms in the lipid head groups.

Stability of a protein during the simulation was assessed by (i) monitoring the time series of atom-positional root-mean-square deviation (rmsd) of all backbone heavy atoms (N, C$_\alpha$, C) from the structure obtained after equilibration after a roto-translational fit of all C$_\alpha$ atoms to this reference structure; (ii) evaluating the time average of the number of backbone hydrogen bonds, based on defining a hydrogen bond *via* a geometric criterion: a maximum hydrogen atom-acceptor distance of 0.25 nm combined with a minimum donor-

hydrogen atom-acceptor angle of 135°; (*iii*) monitoring the time series of fractions of protein residues occurring in secondary structure elements α-helix, 3_{10}-helix, π-helix, or β-sheet, based on secondary structure definitions according to the Kabsch–Sander rules.[87]

For three proteins, the simulated trajectories were also validated against available experimental NMR data, namely, the NOE values of ref 88, ref 57, and refs 59, 89 for HEWL, FOX, and GCN, respectively, and ^3J-coupling constants of ref 88 and refs 59, 89 for HEWL and GCN, respectively. To perform a comparison against upper bounds for interproton distances derived from NOE experiments, an inverse-sixth power averaging was applied to the interproton distances $r_{H_i-H_j}$ monitored during the simulation, i.e.

$$r_{H_i-H_j}^{ave} = \langle r_{H_i-H_j}^{-6} \rangle^{-1/6} \tag{11}$$

where angular brackets indicate an ensemble average. Since the GROMOS force field relies on a united-atom representation of aliphatic CH_n ($n = 1, 2, 3, 4$) groups, the positions of hydrogen atoms which are not treated explicitly were deduced based on geometric criteria.[35] Furthermore, in cases where experimental NOE data refer to stereochemically equivalent and non-stereoassigned protons, pseudoatom positions[90] were constructed according to geometric criteria and were used in combination with corresponding standard GROMOS corrections[35] but without any additional multiplicity corrections.[91] Average NOE violations were calculated as the sum of positive violations divided by the number of available NOE values. To perform a comparison against experimental ^3J-coupling constants between two protons, these quantities were calculated from the simulated trajectory based on the average dihedral angle φ_i formed by the respective set of bonded atoms. Here, exclusively coupling constants $^3J_{H_N-H_\alpha}(\phi_i)$ between backbone amide hydrogen and C_α hydrogen atoms were considered. However, because the aliphatic $H_{\alpha,i}$ hydrogen atom is merged together with the atom $C_{\alpha,i}$ in the GROMOS force field,[35] the dihedral angle ϕ_i' formed by the atoms $C_{i-1}-N_i-C_{\alpha,i}-C_i$ was used instead. The ^3J-coupling constants were calculated from the Karplus relation[92] as

$$^3J_{H_N-H_\alpha}(\phi_i) = A\cos^2\phi_i + B\cos\phi_i + C \tag{12}$$

where $\phi_i = \phi_i' - 60°$ and the parameters of ref 93 were used ($A = 6.4$ Hz, $B = -1.4$ Hz, $C = 1.9$ Hz).

For the simulations of the SAC protein, various pair distribution functions involving charged functional groups were calculated. Radial distribution functions $g_{IJ}(r)$ were calculated for water oxygen atoms, sodium ions, and chloride ions around (*i*) the amino nitrogen atoms of the alkylguanidinium group of arginine residues, (*ii*) the nitrogen atoms of the alkylammonium group of lysine residues, and (*iii*) the carboxylate oxygen atoms of aspartate and glutamate residues, as

$$g_{IJ}(r) = (4\pi\Delta r r^2 \eta_J)^{-1}\langle N_J(r; r_{IJ})\rangle \tag{13}$$

where r_{IJ} denotes the minimum-image distance between groups I and J, η_J is the number density of group J in the system, $\langle N_J(r; r_{IJ})\rangle$ is the average number of groups J with $r - (1/2)\Delta r \leq r_{IJ} < r + (1/2)\Delta r$, and the bin width $\Delta r = 0.01$ nm. Distance probability distributions $P_{I\in\alpha,J\in\beta}^{\alpha\beta}(r)$, $\alpha,\beta = +, -$ denoting the set of charged protein functional groups, were calculated from the distance time series of all pairs of like-charged positive

($P_{I\in+,J\in+}^{++}$), like-charged negative ($P_{I\in-,J\in-}^{--}$), and oppositely charged ($P_{I\in+,J\in-}^{+-}$) protein functional groups. The distance measurements were based on the alkylguanidinium carbon atoms of arginine residues, the alkylammonium nitrogen atoms of lysine residues, and the carboxylate carbon atoms of aspartate and glutamate residues, and the functions $P_{I\in\alpha,J\in\beta}^{\alpha\beta}(r)$ were normalized such that

$$\int_0^\infty dr\, P_{I\in\alpha,J\in\beta}^{\alpha\beta}(r) = N_{pair}^{\alpha\beta} \tag{14}$$

where the number of distinguishable pairs $N_{pair}^{\alpha\beta}$ evaluates to $N_{pair}^{++} = 153$, $N_{pair}^{--} = 66$, and $N_{pair}^{+-} = 216$.

All the above analyses were done with the gromos++ package of programs.[94]

III. RESULTS

III.1. Electrolyte Solutions. Average box volumes monitored during the production runs are reported in Table 2. Kirkwood–Buff integrals $G_{IJ}(L_s^{-1})$ are displayed in Figure 1 for salt–salt, salt–water, and water–water interactions as a
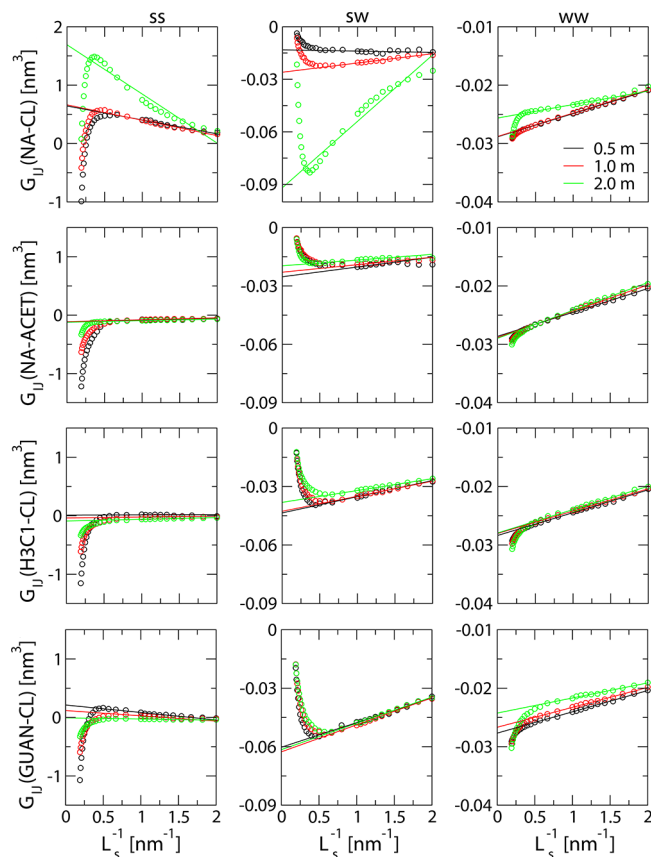
Figure 1. Kirkwood–Buff integrals $G_{IJ}(L_s^{-1})$ for salt–salt (ss), salt–water (sw), and water–water (ww) interactions calculated from MD simulations of the systems listed in Table 2 for salt molalities $b_s = 0.5$ m (black), 1.0 m (red), and 2.0 m (green). Circles represent $G_{IJ}(L_s^{-1})$ evaluated *via* eq 4 using sub-boxes of edge length L_s randomly positioned in computational boxes of average volume $\langle L^3 \rangle$ reported in Table 2. Solid lines represent a linear fit to the linear regime of $G_{IJ}(L_s^{-1})$. The choice of linear regime appears ambiguous for salt–salt and salt–water interactions in 2 m NA-CL, which is why for these systems the fit was performed over the range $L_s^{-1} > L_{s,max}^{-1}$, where $L_{s,max}^{-1}$ denotes the onset of divergent behavior in $G_{IJ}(L_s^{-1})$, i.e., approximately 0.39 nm^{-1} (section III.1).

function of inverse edge length L_s^{-1} of the sub-box (eq 4). Table 2 reports the y-axis intercepts of linear fits to $G_{IJ}(L_s^{-1})$, corresponding to finite-size corrected Kirkwood−Buff integrals. Divergence of $G_{IJ}(L_s^{-1})$ for $L_s^{-1} \to 0$ is due to insufficient size of the particle reservoir surrounding the sub-box. Significant deviations from linearity are observed for $0.5 < L_s^{-1} < 1.0$ nm^{-1} in the case of salt−salt and salt−water Kirkwood−Buff integrals for 2 m NA-CL and $1.5 < L_s^{-1} < 2.0$ nm^{-1} in the case of salt−water Kirkwood−Buff integrals for 2 m NA-CL, which might be caused by spurious ion clustering in this system. From eq 4, it can be seen that excessive pairing between I and J species (i.e., high correlation between N_I and N_J) leads to an increase in G_{IJ}. The increase in the magnitude of the slope of $G_{IJ}(L_s^{-1})$ for $0.5 < L_s^{-1} < 1.0$ nm^{-1} in salt−salt and salt−water Kirkwood−Buff integrals for 2 m NA-CL, which leads to an increase of the salt−salt and a decrease of the salt−water Kirkwood−Buff integrals, is thus indicative of increased interionic and decreased ion−water interactions. Similarly, the slope of $G_{IJ}(L_s^{-1})$ for salt−water interactions in 2 m NA-CL is more negative in the range $1.0 < L_s^{-1} < 1.5$ nm^{-1} than in the range $1.5 < L_s^{-1} < 2.0$ nm^{-1}, which indicates a corresponding loss of ion−water pairing in sub-boxes of the former size. The choice of linear regime is thus ambiguous for salt−salt and salt−water interactions in 2 m NA-CL. Therefore, for these systems, the fit was performed over the range $L_s^{-1} > L_{s,max}^{-1}$, where $L_{s,max}^{-1}$ denotes the onset of divergent behavior in $G_{IJ}(L_s^{-1})$, i.e., approximately 0.39 nm^{-1} (Figure 1). Note that the particular choice of fitting range does not crucially affect f_{ss} for 2 m NA-CL. For example, a fit in the range $0.5 < L_s^{-1} < 1.0$ nm^{-1} leads to $G_{ss} = 1.97$ and $G_{sw} = -0.103$ nm^3, i.e., to results reflecting enhanced ion−ion pairing at the cost of ion−water pairing in comparison to the results obtained from the fit over the range $L_s^{-1} > L_{s,max}^{-1}$ ($G_{ss} = 1.69$ and $G_{sw} = -0.092$ nm^3; Table 2). The f_{ss} values corresponding to the former and latter Kirkwood−Buff integrals differ only marginally (-0.82 and -0.80, respectively; Table 2).

Evaluation of the Kirkwood−Buff integrals G_{IJ} for salt−salt, salt−water, and water−water interactions allows calculation of activity derivatives f_{ss} (eq 2) *via* eq 5. These values, along with corresponding experimental data, are reported in Table 2. Activity derivatives f_{ss} express the change of the activity coefficient f_s with salt concentration. The experimental values of $\ln f_s$ are displayed in Figure 2a as a function of $\ln x_s$. A deviation of $\ln f_s$ from zero indicates nonideality, which, in a salt solution, may be caused by ion pairing (mutual excess coordination of oppositely-charged salt components) or increased water density in the vicinity of ions (excess coordination of salt components by water molecules). An increase in salt concentration is expected to enhance ion pairing and to reduce hydration effects, i.e., to enhance opposing effects on solution ideality. As illustrated in Figure 2a, an increase in the salt mole fraction has a very limited influence on the (mean rational) activity coefficient up to salt mole fractions x_s (eq A.3) of about 0.0177 ($\ln x_s = -4.03$; salt molality $b_s = 0.5$ m) for GUAN-CL, of about 0.0348 ($\ln x_s = -3.36$; $b_s = 1.0$ m) for NA-ACET and of about 0.0672 ($\ln x_s = -2.70$; $b_s = 2.0$ m) for NA-CL and H3C1-CL. The derivatives f_{ss} of $\ln f_s$ with respect to $\ln x_s$ (eq 2) are displayed in Figure 2b as a function of $\ln x_s$ for both the simulated and experimental salt solutions, the corresponding numerical values being reported in Table 2. Simulated and experimental data for f_{ss} are in very good quantitative agreement for salts NA-ACET, H3C1-CL, and GUAN-CL at concentrations up to 1.0 m (mean and maximum absolute deviations from experiment amounting to 0.05 and 0.07,
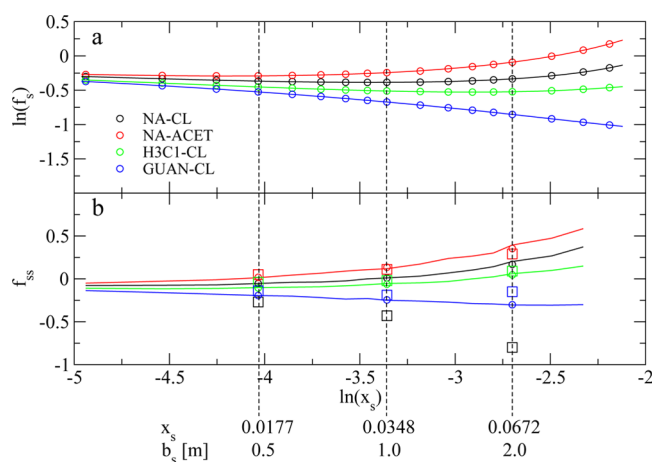
Figure 2. Experimental salt (mean) activity coefficients f_s and experimental and simulated estimates for activity derivatives f_{ss}. (a) Natural logarithm of experimental salt (mean) activity coefficients, $\ln(f_s)$, displayed as a function of the natural logarithm of the salt mole fraction, $\ln(x_s)$. Experimental data (circles) are from ref 79 for NA-CL and NA-ACET, ref 101 for H3C1-CL, and ref 102 for GUAN-CL. The solid lines correspond to the fit of eq A.2. (b) Experimental and simulated activity derivatives f_{ss}. The solid lines are derivatives $((\partial \ln f_s)/(\partial \ln x_s))_{P,T}$ (eq 2) obtained from numerical centered finite differentiation of the experimental data for $\ln(f_s)$ plotted in panel a. Circles denote analogous analytical derivatives at the respective salt mole fractions, obtained from fitted functions (eq A.2), using the fitting coefficients reported in Supporting Information, Table SI. Squares denote simulated results for f_{ss} (Table 2). Dashed vertical lines are a guide for the eye and indicate salt molalities $b_s = 0.5$ m ($x_s = 0.0177$; $\ln x_s = -4.034$), 1.0 m ($x_s = 0.0348$; $\ln x_s = -3.358$), and 2.0 m ($x_s = 0.0672$; $\ln x_s = -2.700$).

respectively), and also for NA-ACET and H3C1-CL at 2.0 m concentration (mean and maximum absolute deviations from experiment amounting to 0.05 and 0.06, respectively), whereas a higher deviation from experimental data is found for GUAN-CL at 2.0 m concentration (0.15). The salts involving oligoatomic ionic species thus reproduce experimental data very well, however, not even qualitative agreement is found for NA-CL throughout the whole range of examined concentrations. For the latter salt, the simulated systems exhibit a drastic increase in nonideality (assuming $\ln f_s < 0$ for $b = 0.5$ m) upon an increase in salt concentration (i.e., the activity derivative f_{ss} is negative for $b = 0.5$ m and becomes more negative upon further increasing the salt concentration, hence leading to a further decrease in f_s), indicating a failure of the GROMOS 54A7 and 54A8 force-field parameter sets to correctly account for the balance between ion−ion and ion−water binding propensities of sodium and chloride ions. Note in this context that the simulations performed here involve ions which are parametrized against methodology-independent hydration free energies but involve forces according to an approximate electrostatic scheme, which, owing to the predominantly negative correction terms, effectively render the ions underhydrated. It can be expected that this underhydration is more severe for cations (negative type-C_1 correction) than for anions (positive type-C_1 correction)[95] and possibly also more severe for monatomic ions (concentrated charge) than for oligoatomic ones (dispersed charge), which may entail an overestimation of ion pairing. Spurious clustering of ions in a 4.5 M aqueous sodium chloride solution was previously observed for the GROMOS and AMBER force

fields, using ion parameters that were not calibrated with a methodologically-independent approach.[42,96]

Cutoff artifacts turned out to significantly affect ion−water and ion−ion pair distribution functions when electrostatic interactions were handled with the Barker−Watts reaction-field scheme (data not shown). In the limit of infinite box-edge lengths, lattice-sum electrostatic interactions are Coulombic, while periodicity-induced artifacts occur with finite box-edge lengths. The authors of the present study assume that the latter artifacts are negligible for the current systems in cubic computational boxes of the size used here (about 6 nm edge length; Table 1).

In view of the nonconsideration of the properties of electrolyte solutions in the parametrization strategy of the GROMOS 54A8 force field,[22] the crude empirical relationship used to calculate heteroatomic Lennard-Jones interaction coefficients in the GROMOS force field (geometric mean combination rule),[35] and the simplicity of the employed water model (rigid three-site model without explicit polarization),[23] it is astonishing that the GROMOS 54A8 force field is capable of accounting for properties of electrolyte solutions involving the oligoatomic ions in the concentration regime up to 1.0−2.0 m. However, the present study only investigated activity coefficient derivatives. Future work will be directed toward a more thorough analysis of the thermodynamic, structural, and dynamic properties of electrolyte solutions.

III.2. Lipid Bilayers. The DPPC bilayers simulated in the present study with the GROMOS 54A8 force field ($DPPC_1$) or with parameter sets differing solely by an increased Lennard-Jones repulsion between choline head groups and phosphate oxygen atoms ($DPPC_2$, $DPPC_3$) remain in the liquid crystalline-like phase, as evidenced by structural properties such as, e.g., area A_L and volume V_L per lipid, bilayer thickness D_{HH} (Table 3) and electron density profiles (Figure 3a). The

Table 3. Area per Lipid A_L (eq 7), Volume per Lipid V_L (eq 8) and Bilayer Thickness D_{HH} Based on the Electron Density Profile Due to Lipid Head Group Atoms (eq 10 and Figure 3b) Evaluated from Simulations $DPPC_1$, $DPPC_2$, and $DPPC_3$[a]

simulation	A_L [nm^2]	V_L [nm^3]	D_{HH} [nm]	$2V_L A_L^{-1}$ [nm]
$DPPC_1$	0.64	1.222	3.74 (3.06)	3.82
$DPPC_2$	0.68	1.227	3.54 (2.86)	3.61
$DPPC_3$	0.71	1.228	3.44 (2.74)	3.46
C3 (54A7)[b]	0.63	1.226	3.57[c]	3.89
exp.[d]	0.629; 0.643	1.229; 1.232	3.42; 3.83	3.82[e]−3.92[f]
exp.[g]	0.64	1.232	3.83	3.85

[a]The values reported in parentheses for D_{HH} refer to the electron density profile due to all lipid atoms (eq 9 and Figure 3a). For comparison, corresponding results obtained by ref 28 with the GROMOS 54A7 force field are also reported. Experimental data are provided in the form of extreme values found after an investigation of various data sources (see also ref 28) along with "best" values reported in the review of ref 54. [b]Results of simulation C3 reported by ref 28 using the GROMOS 54A7 force-field parameter set and a production run of 120 ns. [c]Ref 28 seems to define the position of the head groups from the total hydrated lipid bilayer electron density profile. [d]Extrema of experimental values reported by refs 52−55, refs 53−55, and refs 53−55,103 for A_L, V_L, and D_{HH}, respectively. [e]Value obtained based on A_L = 0.643 nm^2 and V_L = 1.229 nm^3. [f]Value obtained based on A_L = 0.629 nm^2 and V_L = 1.232 nm^3. [g]"Best" values reported in the review of ref 54.
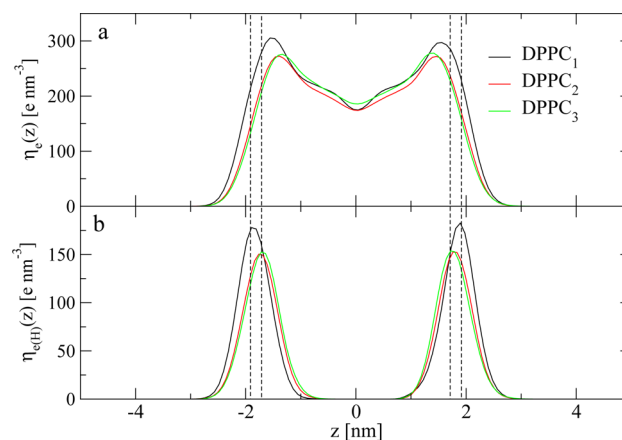
Figure 3. Electron density profile for the DPPC bilayer in simulations $DPPC_1$, $DPPC_2$, and $DPPC_3$. The former corresponds to the GROMOS 54A8 force-field parameter set, whereas the latter two simulations involve increased Lennard-Jones repulsion between the choline head groups and the phosphate oxygen atoms. The dashed lines indicate extreme values for experimentally observed bilayer thicknesses (minimum of[103] 3.42 nm and maximum of[54] 3.83 nm, respectively; see also ref 28 for a compilation of experimental data sources). (a) Electron density profile $\eta_e(z)$ due to all lipid atoms (eq 9). (b) Electron density profile $\eta_{e(H)}(z)$ due to lipid headgroup atoms (eq 10).

average area per lipid from simulation $DPPC_1$ is at the upper threshold of experimentally observed values and equal to the reported "best" value of ref 54 (0.64 nm^2), whereas increased repulsion in the bilayer headgroup moieties renders corresponding values obtained from simulations $DPPC_2$ and $DPPC_3$ somewhat higher (0.68 and 0.71 nm^2, respectively). The average volume per lipid from simulation $DPPC_1$ is slightly underestimated in comparison to experiment (1.222 nm^3 vs 1.229−1.232 nm^3), whereas corresponding values obtained from simulations $DPPC_2$ and $DPPC_3$ are somewhat higher (1.227 and 1.228 nm^3, respectively) and thus in better agreement with experiment (Table 3). The lipid bilayer thickness deduced from the maxima of headgroup atom electron density (eq 10 and Figure 3b) across the bilayer leaflets is within the experimental range for all three DPPC simulations. Assuming an experimental value for D_{HH} of 3.625 nm (arithmetic average between minimum and maximum values of 3.42 and 3.83 nm, respectively; Table 3), simulations $DPPC_1$, $DPPC_2$, and $DPPC_3$ show deviations of 3.2, −2.3, and −5.1%, respectively. However, if the "best" value reported by ref 54 is taken as experimental reference (3.83 nm), simulation $DPPC_1$ shows the smallest deviation (−2.3%). Considering the electron density profile due to all lipid atoms (eq 9 and Figure 3a), the distance between the maxima appears significantly smaller and underestimates the experimental value by 15.6% ($DPPC_1$), 21.1% ($DPPC_2$), and 24.4% ($DPPC_3$). Tentatively approximating a measure of bilayer thickness with $2V_L A_L^{-1}$, the results are similar to corresponding data calculated from experimental A_L and V_L values. Note that the results presented above have to be taken with some caution, because (i) the simulation time scale (40 ns) might not be sufficient to allow full relaxation of lipid bilayer structural properties and exhaustive sampling of long-time scale collective events such as, e.g., undulation movements and (ii) the simulations were performed with a reaction-field electrostatic interaction function, which might cause artifacts in the sampled

Table 4. Parameters Characterizing Stability of Secondary Structure Evaluated from the Indicated Proteins[a]

simulation	rmsd$_{bb}$ (max.) [nm]	N_{bb-hb} (% of ini.)	$f_{\alpha\text{-helix}}$ [%]	$f_{3_{10}\text{-helix}}$ [%]	$f_{\pi\text{-helix}}$ [%]	$f_{\beta\text{-sheet}}$ [%]	N_R	N_K	N_D	N_E
HEWL	0.20 (0.31)	59.1 (89.5)	34.4	3.7	1.7	6.1	11	6	7	2
ini.		66	29.5	14.0	0.8	6.2				
FOX	0.29[b] (0.39)[b]	34.9 (79.3)	17.5	1.5	0.0	21.8	9	5 (6)[c]	5	7
ini.		44	21.6	0.0	0.0	23.9				
CM	0.33 (0.44)	102.3 (87.4)	74.1	2.3	0.0	0.0	14	4	14	9
ini.		117	72.4	6.7	0.0	0.0				
GCN	0.34 (0.55)	8.0 (80.0)	47.3	0.3	16.6	0.0	1	2	0	2
ini.		10	62.5	12.5	0.0	0.0				
PROTG	0.13 (0.32)	29.5 (95.2)	25.9	0.1	0.1	39.1	0	6	5	5
ini.		31	25.0	0.0	0.0	42.9				
COLDS	0.17 (0.29)	30.1 (88.5)	0.0	3.3	0.0	42.1	0	7	6	2
ini.		34	0.0	4.3	0.0	40.6				
SAC$_0^{54A7}$	0.27 (0.37)	28.9 (80.3)	16.0	3.7	0.1	35.7	4	14	5	7
SAC$_0^{54A8}$	0.27 (0.50)	28.9 (80.3)	16.7	3.2	0.0	37.0				
SAC$_{Cl^-}^{54A7}$	0.22 (0.40)	27.7 (76.9)	16.7	0.6	0.0	34.7				
SAC$_{Cl^-}^{54A8}$	0.28 (0.45)	28.5 (79.2)	18.9	2.5	0.0	31.6				
SAC$_{NaCl}^{54A7}$	0.23 (0.34)	29.4 (81.7)	17.9	2.4	0.1	36.0				
SAC$_{NaCl}^{54A8}$	0.36 (0.52)	25.8 (71.7)	13.2	2.8	0.0	34.4				
ini.		36[d]	21.2[d]	9.1[d]	0.0[d]	45.5[d]				

[a]The reported data include the average backbone heavy atom−positional rmsd from the structure obtained after equilibration, rmsd$_{bb}$, evaluated after fitting the backbone C$_\alpha$ atoms to this structure, as well as the maximum instantaneous rmsd value in parentheses, the average number of backbone hydrogen bonds N_{bb-hb}, as well as the corresponding fraction of the initial number of backbone hydrogen bonds in parentheses, and average fractions $f_{\alpha\text{-helix}}$, $f_{3_{10}\text{-helix}}$, $f_{\pi\text{-helix}}$, and $f_{\beta\text{-sheet}}$ of protein residues occurring in secondary structure elements α-helix, 3_{10}-helix, π-helix, or β-sheet, respectively. Table entries "ini." denote data corresponding to the initial (minimized) structures. In addition, the number of charged arginine (N_R), lysine (N_K), aspartate (N_D), and glutamate (N_E) side chains is reported. [b]Considering residues 9−82 only (the rmsd of the backbone atoms of all residues, i.e. residues 1−88, is significantly higher due to large fluctuations in the tail regions and its average and maximum values evaluate to 0.54 and 0.68 nm, respectively). [c]The FOX protein contains six lysine residues, of which only five were protonated to maintain consistency with previous studies involving this protein,[21,63] where the deprotonation of this residue was erroneously introduced (section II.1.3). [d]This number turns out to be the same regardless of whether the minimization of the system was performed with the GROMOS 54A7 or 54A8 force-field parameter set.

distribution of distances between charged groups. In the study of ref 28, some results of which are also reported in Table 3 for comparison, a production run of 120 ns length and a lattice-sum electrostatic interaction function was used to simulate a DPPC bilayer with the GROMOS 54A7 force field. Both A_L and D_{HH} agree with experimental values, whereas V_L is slightly underestimated.

The Lennard-Jones repulsion coefficient $C_{12,ij}$ for interactions between the united-atom methyl groups of the choline head groups and phosphate oxygen atoms evaluates to 6.93×10^{-6}, 1.48×10^{-5}, 2.47×10^{-5}, and 1.58×10^{-5} kJ·mol^{-1}·nm^{12} in simulations DPPC$_1$, DPPC$_2$, and DPPC$_3$ and the GROMOS 54A7 force field, respectively, so that actually the force-field parameter set employed in simulation DPPC$_2$ is most similar to the GROMOS 54A7 force field. However, the results obtained in the present study (Table 3) give better agreement with experimental values in the case of DPPC$_1$ concerning A_L, D_{HH} and $2V_LA_L^{-1}$. This difference is most likely caused by the usage of a different electrostatic interaction function. It has been pointed out before that A_L is very sensitive to simulation methodology, in particular, to the treatment of long-range electrostatic interactions.[97] Notably, larger A_L values were found before with a reaction-field electrostatic interaction function than with a lattice-sum electrostatic interaction function.[97] Since it is difficult to assess the relative merits of different electrostatic interaction functions in the absence of an "ideal" reference characterized by macroscropic nonperiodic extent and Coulombic electrostatic interactions, and since the parametrization of the GROMOS force field relies on a truncated electrostatic interaction function with a Barker−

Watts reaction-field correction, simulation DPPC$_1$ is still considered to provide the most reasonable area per lipid in the present context.

Time evolutions of A_L and V_L during the production runs are shown in Supporting Information Figures S1 and S2. While simulations DPPC$_2$ and DPPC$_3$ present a sharp initial increase in A_L, simulation DPPC$_1$ shows a rather stable area per lipid around 0.64 nm^2. The volume per lipid V_L exhibits less pronounced fluctuations than A_L. It has been suggested before that V_L might therefore be a more suitable property for the purpose of force-field calibration or/and validation.[28] However, its calculation involves an estimate for the effective volume of a water molecule (eq 8), evaluated from the simulation of a pure water system. The authors of the present study think that it might not be appropriate to use such an estimate for water in the presence of a lipid bilayer, because solvent electrostriction effects in the vicinity of the charged head groups will not be properly accounted for.

III.3. Proteins. *III.3.1. Secondary Structure Stability.* As evidenced by quantitative structural characteristics of secondary structure elements, such as, e.g., the number of backbone hydrogen bonds N_{bb}, the rmsd of the backbone from a representative reference structure rmsd$_{bb}$, or the fraction of residues present in given secondary structure elements, the proteins simulated in the present study remain structurally intact (Table 4). This is not surprising because (i) the suitability of the GROMOS 54A7 force field for protein simulation has been previously validated[21] and (ii) the sole difference between the GROMOS 54A7 and 54A8 force fields is in the description of charged amino acid side chains, and it is
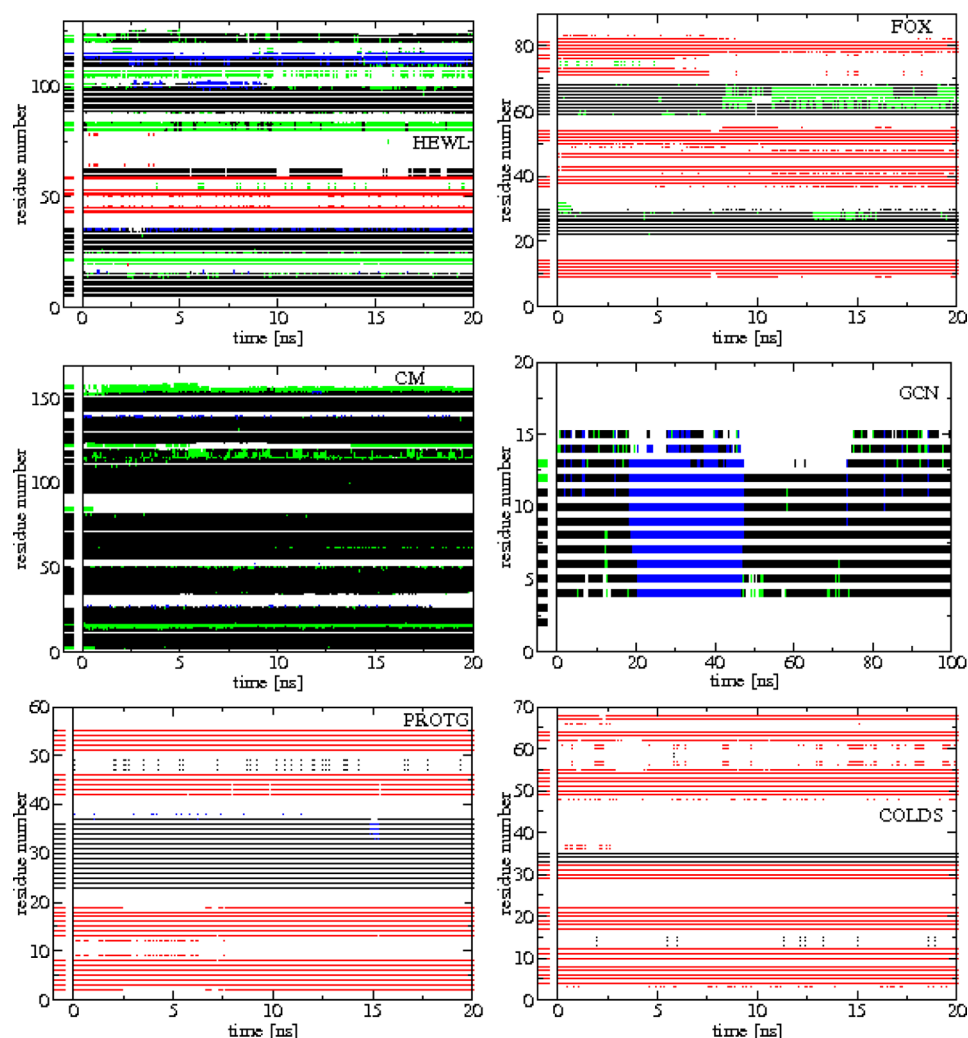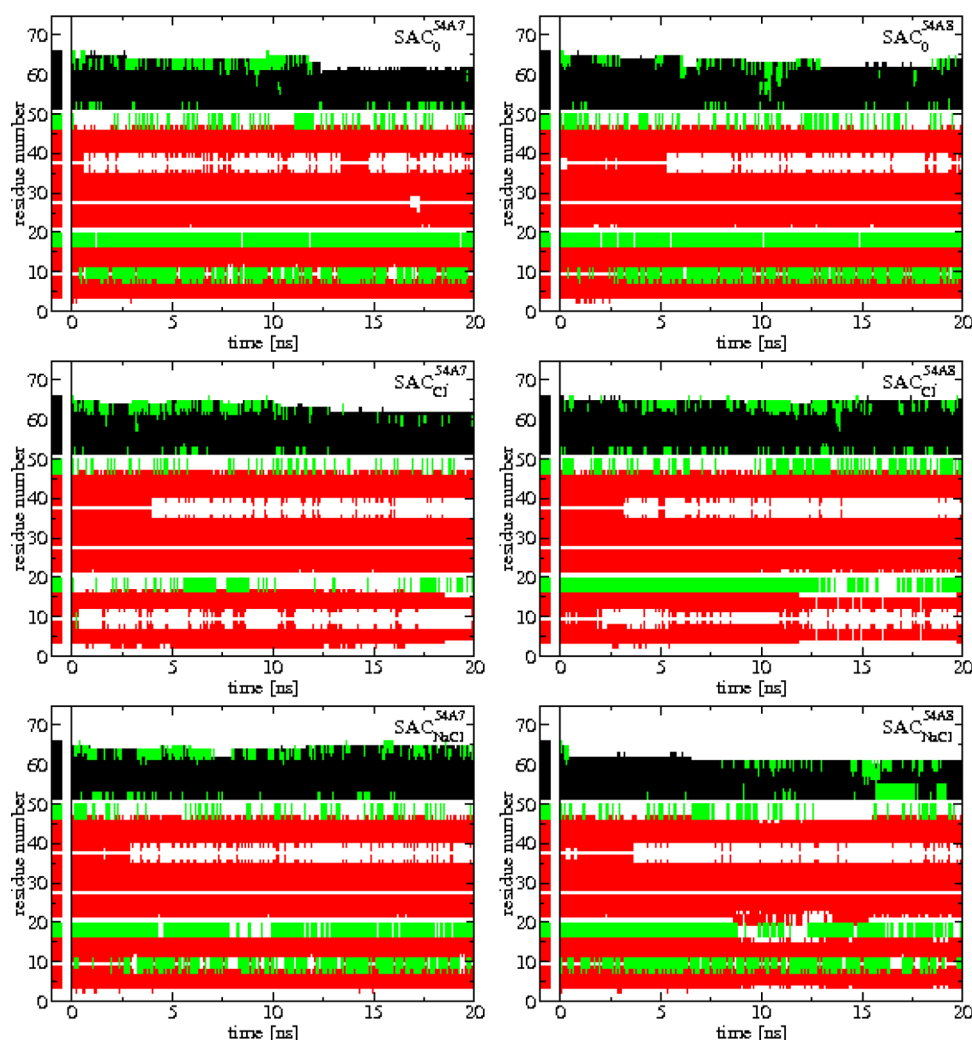
Figure 4. Residues occurring in secondary structure elements α-helix (black), 3_{10}-helix (green), π-helix (blue), or β-sheet (red) during the simulations of HEWL, FOX, CM, GCN, PROTG, and COLDS. Secondary structure elements of the initial (minimized) structure are indicated in the short stretch at the left-hand side of each graph.

known that intramolecular salt bridges influence protein stability only marginally.[43−46] As can be seen from Table 4, the average backbone rmsd values $rmsd_{bb}$ of all proteins are within 0.36 nm of the initial structure. PROTG and COLDS exhibit exceptional stability, with $rmsd_{bb}$ values of 0.13 and 0.17 nm, respectively. The highest value is found for SAC_{NaCl}^{54A8} (0.36 nm) and can be drawn back to a movement of the last ca. seven C-terminal residues (see below). For FOX, the reported $rmsd_{bb}$ value refers to residues 9−82 only. This protein has extremely flexible terminal tails, and the $rmsd_{bb}$ calculated for the whole protein (residues 1−88) amounts to 0.54 nm. The time evolutions of $rmsd_{bb}$ values are provided in Supporting Information Figure S3 and also illustrate that deviations from the initial structure in FOX can mainly be ascribed to structural fluctuations occurring at the termini.

On average, the initial number of backbone hydrogen bonds is maintained up to 86.7% in simulations HEWL, FOX, CM, GCN, PROTG, and COLDS, respectively, and 78.4% in simulations SAC_0^{54A7}, SAC_0^{54A8}, $SAC_{Cl^-}^{54A7}$, $SAC_{Cl^-}^{54A8}$, SAC_{NaCl}^{54A7}, and SAC_{NaCl}^{54A8}, respectively. These values are relatively high (>75%), i.e., indicative of an overall secondary structure close to the initial one, with the exception of SAC_{NaCl}^{54A8} where the C-terminal tail formed by residues 60−66 (RAEREKK) moves at the

beginning of the simulation. This is reflected by an increased root-mean-square fluctuation (rmsf) of the corresponding C_α atoms (the average C_α rmsf values of residues 1−59 and 60−66 are 0.19 and 0.40 nm, respectively), an associated loss of α-helical structure (Figure 5), and the fact that the average backbone rmsd obtained upon the omission of the seven terminal residues from the calculation is lower than the value of 0.36 nm reported in Table 4, and more similar to the values found for the other SAC simulations, namely 0.31 nm. Visual inspection of the coordinate trajectory suggests that the tail movement is accidental (or water-driven; see, however, below), because it could not be correlated with any other obvious event such as, e.g., counterion binding. The possibly most crucial change between the GROMOS 54A7 and 54A8 force fields affects the carboxylate side chains, which are more hydrophilic by about 40 kJ·mol^{-1} in the latter parameter set. Therefore, one might feel tempted to ascribe an increased flexibility of the tail to the hydration properties of the glutamate side chains E62 and E64 and the carboxylate terminus of K66. This is, however, unlikely, because the α-helical tail structure is e.g. maintained throughout simulation $SAC_{Cl^-}^{54A8}$ and is affected by similar stability problems toward the end of simulations SAC_0^{54A7} and $SAC_{Cl^-}^{54A7}$ (Figure 5).

Figure 5. Residues occurring in secondary structure elements α-helix (black), 3_{10}-helix (green), π-helix (blue), or β-sheet (red) during the simulations of SAC_0^{54A7}, SAC_0^{54A8}, $\mathrm{SAC}_{Cl^-}^{54A7}$, $\mathrm{SAC}_{Cl^-}^{54A8}$, $\mathrm{SAC}_{NaCl}^{54A7}$, and $\mathrm{SAC}_{NaCl}^{54A8}$. Secondary structure elements of the initial (minimized) structure are indicated in the short stretch at the left-hand side of each graph.

Besides monitoring backbone hydrogen bonds, other indications of stable secondary structure are the average fractions of protein residues in given secondary structure elements. Overall, these values are also close to those characterizing the initial structure. In combination with visual inspection of the coordinate trajectories or/and the time evolution of secondary structure elements (Figures 4 and 5), this suggests the absence of a severe spurious structural bias in the underlying force field. The most striking secondary structural changes are an increase in α-helix content of HEWL and CM; a decrease in α-helix content of GCN and SAC; a decrease in 3_{10}-helix content of HEWL, CM, GCN, and SAC; an increase in π-helix content of GCN; an increase in β-sheet content of COLDS; and a decrease in β-sheet content of SAC. Clearly, in HEWL and CM, there is transformation between 3_{10}- and α-helices, and in GCN, there is a transformation between a π- and an α-helix. The 3_{10}-helices formed by residues 120−123 of HEWL and 2−3 of CM convert to α-helices after about 1.7−2.2 and 0.6 ns, respectively, and largely retain this conformation during the remainder of the simulation time. It was suggested before[21] that the GROMOS 54A7 force field marginally overstabilizes α-helices in comparison to 3_{10}-helices, and the same finding appears to

hold for the GROMOS 54A8 force field. On the contrary, the transformation to a π-helix in the GCN peptide after about 20 ns seems to be more transient since the α-helical conformation is recovered after about 45 ns. For FOX, one can recognize a loss of β-sheet (residues 71−73) after about 7.4 ns. This is not severe because the compatibility with experimental NOE values is still ensured (see below).

The SAC protein seems to be somewhat less stable than the other proteins, which can, to a certain extent, be drawn back to the flexibility of the last ca. seven C-terminal residues, which is also qualitatively reflected in the reported "B-factors" of the NMR structure. Note also that the SAC protein is native to a hyperthermophilic organism (Table 1). At elevated temperatures, the solvation properties of water are considerably different from those at 300 K, i.e., due to a decrease in relative dielectric permittivity, water becomes less solvating. This enhances protein stability at high temperatures (enhanced salt-bridge formation). A limited loss of secondary structure elements at 300 K as encountered in the present study might therefore not be observed in simulations under the physiological conditions of the hyperthermophile species *Sulfolobus acidocaldarius*. However, no such simulations were undertaken because the temperature dependence of the relative
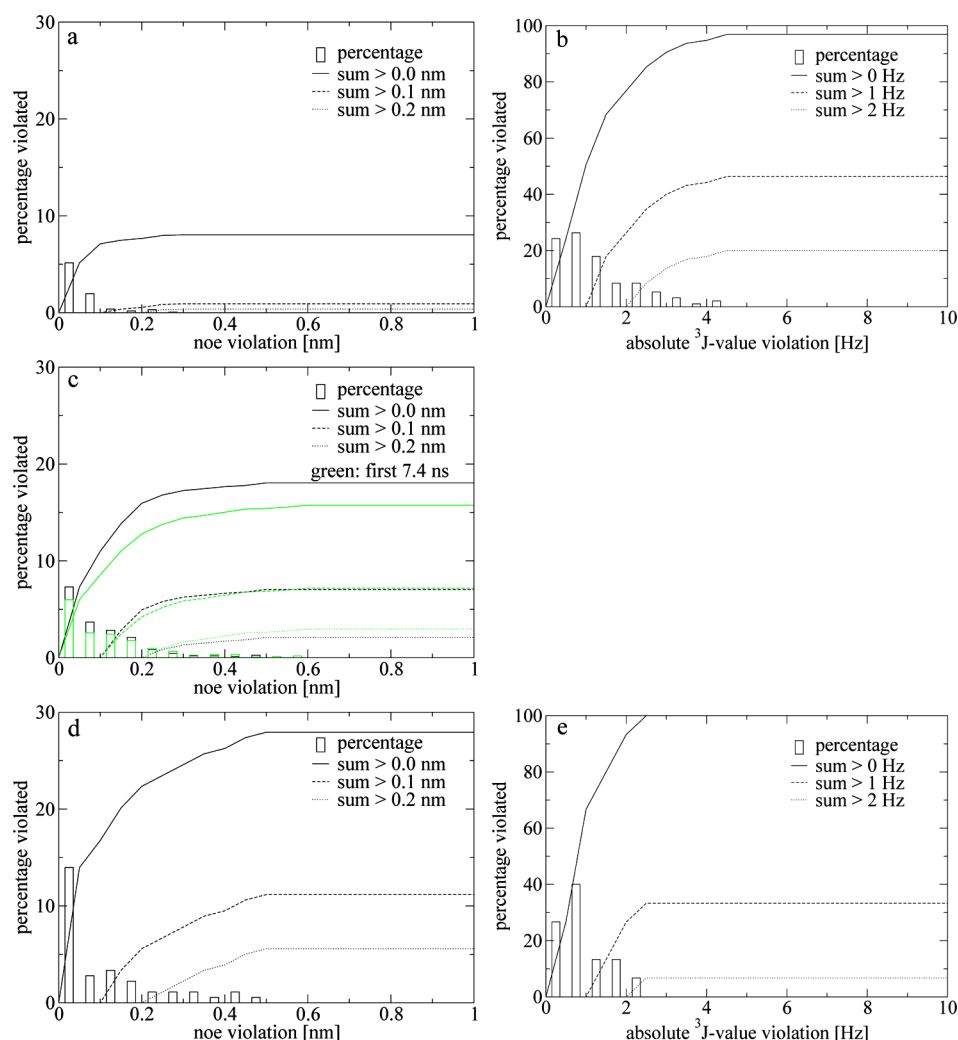
Figure 6. Comparison of the simulations of HEWL (a, b), FOX (c), and GCN (d, e) with experimental NMR data in terms of NOE values (a, c, d) and ^3J-coupling constants (b, e; HEWL and GCN only). Bar diagrams depict the fractions of violations in bins of 0.05 nm (NOE values) or 0.5 Hz (^3J-coupling constants), where corresponding bars are drawn at the bin center locations. The fractions rely on a total of 1630, 1518, and 179 NOE values for HEWL, FOX, and GCN, respectively, as well as 95 and 15 ^3J-coupling constants for HEWL and GCN, respectively. The lines represent cumulative sums of the fractions of violations. For FOX, additional cumulative sums obtained from the first 7.4 ns of the simulation are shown in green color. Note that for NOE values, violations refer to positive deviations, whereas for ^3J-coupling constants, violations refer to absolute deviations from the experimental data. For the latter, deviations with a magnitude of less than 0.1 Hz were defined as zero deviations (three occurrences).

dielectric permittivity of the SPC water model does not quantitatively reproduce the experimental behavior (data not shown). The structural flexibility observed in MD simulations might merely be in keeping with the common notion that structures deposited in the PDB are not necessarily representative of the entire configurational ensemble sampled by the protein in the course of time.

In the SAC protein (Figure 5), a loss of α-helical structure at the C-terminus is found for SAC_0^{54A7}, $SAC_{Cl^-}^{54A7}$, SAC_0^{54A8}, and SAC_{NaCl}^{54A8}. It is likely due to the flexibility of the termini, which is not accounted for by the single structure deposited in the PDB. Moreover, all SAC simulations present a transient formation/deformation of a 3_{10}-helix (residues 47−49) present in the NMR structure. In simulation $SAC_{Cl^-}^{54A7}$, another 3_{10}-helix is similarly destabilized (residues 17−19). No clear-cut differences can be observed depending on the counterion concentration. Overall, the SAC protein seems to have more pronounced flexibility in its secondary structure than the other proteins examined in the present study.

Experimental NMR data in the form of NOE values and ^3J-coupling constants is available for HEWL, FOX (NOE values only), and GCN. For all three proteins, the upper thresholds derived from the NOE values are satisfied to a good extent during the simulations (Figure 6a, c, d), corresponding violations being similar to those observed previously in simulations using the GROMOS 54A7 force field[21] (note the erroneous reporting of violations for GCN in Figure 11 of ref 21). Furthermore, it can be seen that the loss of β-sheet in the FOX protein after about 7.4 ns does not affect the quality of NOE upper bound fulfillment. Nine (first 7.4 ns) or 18 (whole simulation) of 79 NOE values involving at least one of residues 71, 72, and 73 show violations, with average and maximum values of 0.011 and 0.25 nm, respectively, during the first 7.4 ns and 0.018 and 0.23 nm, respectively, during the whole simulation. Violations of experimental ^3J-coupling constants between backbone hydrogen atoms are of similar magnitude to those observed previously in simulations using the GROMOS 54A7 force field[21] (note the erroneous reporting of violations

for HEWL in Figure 5 of ref 21). In general, ^3J-coupling constants are reproduced less well than NOE values (Figure 6b, e), which is mostly due to (*i*) the empirical nature of the relationship between simulated dihedral angles and corresponding deduced ^3J-coupling constants (eq 12), giving rise to uncertainties of up to 1 Hz in the calculated values; (*ii*) insufficient configurational sampling in the present simulations in comparison to the time scales experimental ^3J-coupling constants are averaged over; (*iii*) inaccurate experimental data in the case of GCN.[89] In particular, as attested by the investigation of backbone hydrogen bonds and secondary structure stability (Table 4 and Figure 4), proteins HEWL and GCN appear stable despite the indication of severe violations of experimental data by the backbone hydrogen ^3J-coupling constants.

III.3.2. Salt-Bridge Formation and Counterion Binding Properties. As it is single-ion hydration free energies of charged amino acid side chain analogs which distinguish the GROMOS 54A8 force field from its predecessor 54A7, the thermodynamic equilibrium between salt-bridge formation and hydration of counterions as well as of charged functional groups at the protein surface might be shifted. Possible differences would be reflected in the configurational sampling of distances between charged groups and between charged groups and the solvent, as well as of the orientations of these moieties with respect to each other. However, counterion distributions around (bio)-molecules are often difficult to converge due to relatively slow diffusion of the ions. This is why explicit addition of counterions is sometimes omitted, as, e.g., done in a previous simulation study of the SAC protein.[98] The authors of the present study deem the performed 20 ns simulations sufficiently long to assess possible differences in configurational sampling of charged groups between the GROMOS 54A7 and 54A8 force-field descriptions.

Configurational sampling of the ionic and solvent groups of interest can be characterized by probability distribution functions or/and the averages and fluctuations of corresponding time series. Here, distance probability distributions between charged groups and between charged groups and the solvent were chosen to detect possible consequences of the alternate representation of charged amino acid side chains. Figure 7 depicts radial distribution functions $g_{IJ}(r)$ (eq 13) of the number density of water oxygen atoms, sodium ions, and chloride ions around arginine, lysine, aspartate, and glutamate residues of the SAC protein in simulations $SAC^{54A7}_{Cl^-}$, $SAC^{54A8}_{Cl^-}$, SAC^{54A7}_{NaCl}, and SAC^{54A8}_{NaCl}. It can be seen that using the GROMOS 54A8 force field in comparison to the GROMOS 54A7 force field (*i*) the water number density is enhanced around lysine, aspartate, and glutamate residues, water molecules approach the charged functional groups of arginine and lysine residues more closely, and the first hydration shell of the terminal guanidinium group in arginine residues is tighter, i.e., the corresponding peak is less broad; (*ii*) the number density of sodium ions is reduced around arginine residues and enhanced around aspartate and glutamate residues, whereas it is very similar around lysine residues; (*iii*) the number density of chloride ions is enhanced around arginine and lysine residues and decreased around aspartate and glutamate residues, and chloride ions approach the charged functional groups of arginine and lysine residues more closely. These effects are to be expected based on the stronger hydration of guanidinium and acetate ions in the GROMOS 54A8 force field (due to charge enhancement). The situation is somewhat more complex in the case of the lysine
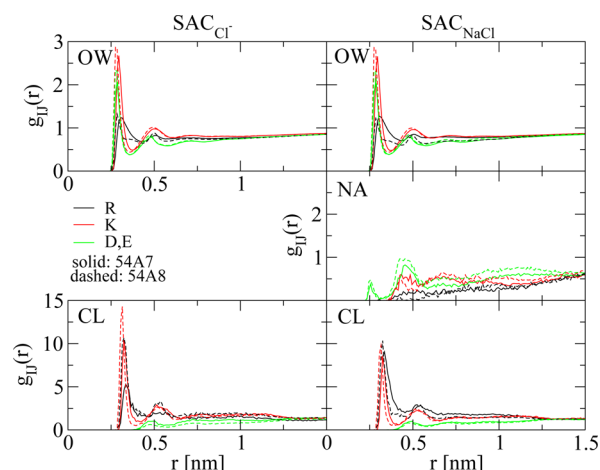

Figure 7. Radial distributions $g_{IJ}(r)$ (eq 13) of the number density of water oxygen atoms (OW), sodium ions (NA), and chloride ions (CL) around arginine (black), lysine (red) as well as aspartate and glutamate (green) residues of the SAC protein in simulations involving solely a neutralizing amount of chloride counterions (SAC_{Cl^-}) or a neutralizing amount of chloride counterions in combination with an equimolar sodium chloride solution (SAC_{NaCl}). The distance measurements are based on the nitrogen atoms of the alkylguanidinium group of arginine residues, the nitrogen atoms of the alkylammonium group of lysine residues, and the carboxylate oxygen atoms of aspartate and glutamate residues. A bin width of 0.01 nm was used in the calculation of $g_{IJ}(r)$. Solid and dashed lines refer to simulations with the GROMOS 54A7 ($SAC^{54A7}_{Cl^-}$, SAC^{54A7}_{NaCl}) and 54A8 ($SAC^{54A8}_{Cl^-}$, SAC^{54A8}_{NaCl}) force field, respectively.

side chain, the small-molecule analog of which is the methylammonium ion in the parametrization procedure. The hydration free energy of this ion is (approximately) the same in the GROMOS 54A7 and 54A8 force-field parameter sets. Nevertheless, the force-field representation of this ion is not the same in both parameter sets. While the distribution of partial atom charges is rather similar, the methyl group Lennard-Jones radius was increased whereas the nitrogen Lennard-Jones radius was decreased upon introduction of the GROMOS 54A8 force-field version.[22] The lysine side chain in the GROMOS 54A8 force field did not adopt a larger Lennard-Jones radius for the methylene group attached to the side-chain nitrogen atom. Therefore, the lysine side chain might in reality be somewhat overhydrated. This explains the above findings of increased water and chloride ion number density around this residue.

Figure 8 depicts normalized (eq 14) probability distribution functions $P^{\alpha\beta}_{I\in\alpha,J\in\beta}(r)$ of the (minimum-image) distance of all pairs of like-charged positive, like-charged negative, and oppositely-charged protein functional groups of the SAC protein in simulations SAC^{54A7}_0, SAC^{54A8}_0, $SAC^{54A7}_{Cl^-}$, $SAC^{54A8}_{Cl^-}$, SAC^{54A7}_{NaCl}, and SAC^{54A8}_{NaCl}. The curves obtained from the two force-field parameter sets are very similar. Considering first peak positions and heights, only marginal differences can be observed, i.e., using the GROMOS 54A8 force field in comparison to the GROMOS 54A7 force field, it appears that the first peak of the distance probability distribution (*i*) between like-charged positive protein functional groups is higher in simulations without counterions or solely a neutralizing amount of chloride counterions, whereas peak positions are unchanged; (*ii*) between like-charged negative protein functional groups is somewhat higher and followed by an immediate second peak in the simulation without counterions, is smaller in the simulation with solely a neutralizing
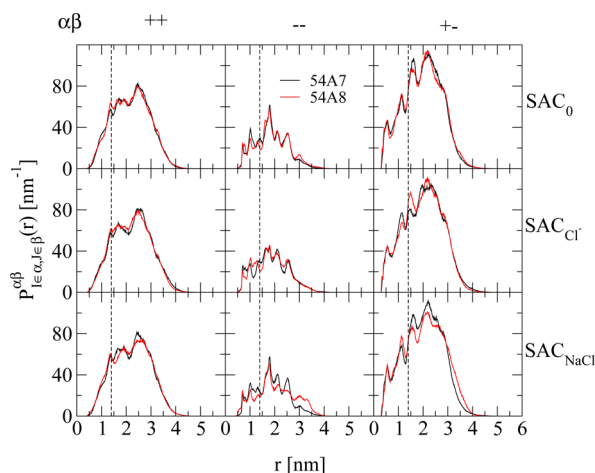
Figure 8. Probability distributions $P^{\alpha\beta}_{I\in\alpha, J\in\beta}(r)$ (section II.3.2) of the (minimum-image) distance of all pairs of like-charged positive ($\alpha = +$, $\beta = +$), like-charged negative ($\alpha = -$, $\beta = -$), and oppositely-charged ($\alpha = +$, $\beta = -$) protein functional groups of the SAC protein in simulations involving no counterions (SAC$_0$), solely a neutralizing amount of chloride counterions (SAC$_{Cl-}$), or a neutralizing amount of chloride counterions in combination with an equimolar sodium chloride solution (SAC$_{NaCl}$). The functions are normalized to integrate to the number of distinguishable pairs (eq 14). The distance measurements are based on the alkylguanidinium carbon atoms of arginine residues, the alkylammonium carbon atoms of lysine residues, and the carboxylate carbon atoms of aspartate and glutamate residues. A bin width of 0.01 nm was used in the calculation of $P^{\alpha\beta}_{I\in\alpha, J\in\beta}(r)$. Black and red lines refer to simulations with the GROMOS 54A7 (SAC$_0^{54A7}$, SAC$_{Cl-}^{54A7}$, SAC$_{NaCl}^{54A7}$) and 54A8 force field (SAC$_0^{54A8}$, SAC$_{Cl-}^{54A8}$, SAC$_{NaCl}^{54A8}$), respectively. The dashed vertical lines indicate an interionic distance of 1.4 nm, i.e., the cutoff distance employed during configurational sampling with the Barker−Watts reaction-field scheme (section II.2).

amount of chloride counterions and is smaller but occurs at a considerably shorter distance in the simulation containing a neutralizing sodium chloride solution; (*iii*) between oppositely-charged protein functional groups is not affected. Note that, overall, the shape of the probability distributions involving like-charged positive and oppositely-charged protein functional groups are extremely similar, whereas the probability distributions involving like-charged negative protein functional groups present more variation between the two different force fields, especially in the simulations containing a neutralizing sodium chloride solution (SAC$_{NaCl}^{54A7}$, SAC$_{NaCl}^{54A8}$). The SAC protein carries a net charge of +6e (Table 4), and therefore, presumably, probability distribution features concerning the separation of positive charges and the formation of salt-bridged ion pairs converge quicker than features concerning the separation of negative charges. Due to possible convergence issues, the latter should therefore be taken with some caution. The equivalence of the distance probability distributions involving oppositely-charged protein functional groups, in particular, the occurrence of an equally high salt-bridged ion-pair peak at a distance of 0.56 nm, is not surprising because potential of mean force calculations as a function of interionic separation of the corresponding charged side chain analogs in water were already found to be rather similar.[22]

Finally, it should be pointed out that distance probability distributions involving charged species will be affected by the use of an approximate electrostatics scheme. A cutoff-truncated effective electrostatic interaction function with a Barker−Watts reaction-field correction was previously shown to provoke the

appearance of a spurious maximum just below and of a spurious minimum just above the cutoff distance in the potential of mean force between oppositely-charged ion pairs in a homogeneous dielectric of a relative permittivity corresponding to that of water.[99,100] The same phenomenon is observed in Figure 8, where a minimum and a maximum in the distance probability distribution between oppositely-charged protein functional groups are observed just below and above the cutoff distance of 1.4 nm, respectively. Similar artifacts can be found in the potential of mean force between like-charged ion pairs.[99,100] Most importantly, the cutoff-induced artifacts turned out to be of significant magnitude in comparison to the thermal energy,[99,100] and it should thus be kept in mind that the distance probability distributions presented in Figure 8 are likely to involve artifacts in side-chain configurational sampling due to the usage of approximate electrostatic interactions.

IV. CONCLUSION

The present study investigated the ability of the GROMOS 54A8 force field to accurately model the structural properties of lipid bilayers, proteins, and electrolyte solutions. Its aim was 4-fold (points *i−iv* in section I), and the conclusions reached in this study can be summarized as follows:

(*i*) Concerning aqueous electrolyte solutions involving ionic species parametrized against methodology-independent hydration free energies, a realistic description of the thermodynamic equilibrium between ion−ion and ion−water pairing propensities in the GROMOS 54A8 force field is not *a priori* guaranteed due to electrostatic artifacts in configurational sampling, the crude empirical relationship used to calculate heteroatomic Lennard-Jones interaction coefficients in the GROMOS force field, and the simplicity of the employed water model. Here, it was assumed that the present simulations of electrolyte solutions with lattice-sum electrostatic interactions are free of periodicity-induced artifacts in cubic computational boxes of about 6 nm edge length. Salts involving oligoatomic species (NA-ACET, GUAN-CL, H3C1-CL) are found to reproduce experimental salt activity derivatives for concentrations up to 1.0 m very well, and good agreement between simulated and experimental data is also found for NA-ACET and H3C1-CL at 2.0 m concentration. However, not even qualitative agreement is found for NA-CL throughout the whole range of examined concentrations, indicating a failure of the GROMOS 54A7 and 54A8 force-field parameter sets to correctly account for the balance between ion−ion and ion−water binding propensities of sodium and chloride ions.

(*ii*) Concerning lipid bilayers, the GROMOS 54A8 force field differs from its predecessor 54A7 by a modified Lennard-Jones repulsion between the choline head groups and the phosphate oxygen atoms. It is found that the GROMOS 54A8 force field reproduces the liquid crystalline-like phase of a hydrated DPPC bilayer at a pressure of 1 bar and a temperature of 323 K. The area per lipid is in agreement with experimental data, whereas other structural properties (volume per lipid, bilayer thickness) appear slightly underestimated. Considering area per lipid estimates from MD simulation, the strong dependence on simulation methodology, in particular, the treatment of long-range electrostatic interactions, should be kept in mind. The present study used truncated electrostatic interactions with a Barker−Watts reaction-field correction for the simulation of lipid bilayers, and it is likely that a slightly lower area per lipid value will be obtained with a lattice-sum electrostatic interaction function.

(*iii*) Concerning proteins, the GROMOS 54A8 force field differs from its predecessor 54A7 in the description of charged amino acid side chains. A range of different proteins was simulated at pH 7, i.e., with all arginine, lysine, aspartate, and glutamate residues carrying net charges. The secondary structure of these proteins is largely maintained and found compatible with experimental NMR data (NOE values and ^3J-coupling constants; where available), which is not surprising because a putatively different thermodynamic equilibrium between salt-bridge formation and hydration of charged functional groups at the protein surface introduced by the new description of charged amino acid side chains is expected to influence protein stability only marginally.[43−46] It should be pointed out that, as was observed for the GROMOS 54A7 force field,[21] the GROMOS 54A8 force field appears to slightly overstabilize α-helices in comparison to 3_{10}-helices.

(*iv*) Concerning proteins in aqueous electrolyte solutions, it appears also important to investigate whether usage of the GROMOS 54A8 force field leads to an altered counterion binding behavior and, as a consequence thereof, a possible impact on salt-bridge formation between charged side chains at the protein surface. On the basis of the law of "matching water affinities",[40,47,48] it cannot *a priori* be ruled out that the counterion distribution around charged protein residues will be affected by the different hydration properties of these residues. Indeed, slight differences in the radial distribution functions of water molecules, sodium and chloride counterions around protein charged functional groups are detected, which can be explained based on the different hydration properties of the corresponding ionic side chain analogs. On average, the side chains of arginine, lysine, aspartate, and glutamate residues appear slightly more hydrated and present a slight excess of oppositely-charged solution components in their vicinity. Salt-bridge formation properties between charged residues at the protein surface, as assessed by probability distributions of interionic distances, are largely equivalent in both force fields. Considering configurational sampling of charged moieties in MD simulation, the strong dependence on the treatment of long-range electrostatic interactions should be kept in mind.

Overall, the authors of the present study think that the 54A8 parameter set of the GROMOS force field can be applied in (bio)molecular simulations of electrolyte solutions, lipids, and proteins, as well as mixtures thereof. Comparison in the context of protein and lipid simulations with its predecessor 54A7 suggests comparable performance. Since the charged functional groups in the GROMOS 54A8 parameter set are derived from a rigorous comparison to single-ion hydration free energies, this parameter set is considered an important step in the continuous development of the GROMOS force field.

■ APPENDIX

Rational activity coefficients f_s (eq 1) can be computed from tabulated data for molal activity coefficients γ_s as[79]

$$f_s = \gamma_s(1 + \nu b_s M_w) \tag{A.1}$$

where b_s is the salt molality, M_w is the molar weight of water $(18.02 \times 10^{-3}\ \text{kg·mol}^{-1})$, and ν is the number of ions generated by dissociation of one salt entity, i.e., $\nu = 2$ for a 1:1 electrolyte.

Experimental data for f_s as a function of b_s was fitted to an equation which derives from expressing the excess molar Gibbs free energy according to the fitted function proposed by Redlich and Kister[104] (term in brackets in eq A.2), augmented

by two additional terms introduced by Guggenheim[105] to satisfy Debye−Hückel theory in the low-concentration limit (last two terms in eq A.2), namely[86]

$$\ln f_s = \beta[-2(a + 3b)x_s + (a + 9b)x_s^2 - 4bx_s^3]$$
$$+ c\frac{\sqrt{I}}{\sqrt{b^\circ} + \sqrt{I}} + dI \tag{A.2}$$

where $b^\circ = 1\ \text{mol·kg}^{-1}$, $\beta = (k_B T)^{-1}$, k_B being Boltzmann's constant, the salt mole fraction x_s defined as[86]

$$x_s = \frac{\nu b_s}{\nu b_s + M_w^{-1}} \tag{A.3}$$

and the ionic strength I used here for simplicity in terms of molal rather than molar concentration (thus avoiding the specification of solution volumes for each salt molality), i.e.,

$$I = 0.5\sum_i b_i z_i^2 \tag{A.4}$$

which is then, for a 1:1 electrolyte, given by

$$I = b_s = -\frac{x_s}{M_w(2x_s - 2)} \tag{A.5}$$

The fit was performed based on 18 data points using experimental data for rational activity coefficients f_s, which were obtained from eq A.1 applied to corresponding molal activity coefficients γ_s of ref 79 for NA-CL and NA-ACET, ref 102 for GUAN-CL, and ref 101 for H3C1-CL for salt molalities of 0.1−1.0 m in steps of 0.1 m, 1.2−2.0 m in steps of 0.2 m, and 2.5−3.5 m in steps of 0.5 m. The resulting coefficients a, b, c, and d are listed in Supporting Information Table SI.

The activity derivative f_{ss} is given by

$$f_{ss} = \left(\frac{\partial \ln f_s}{\partial \ln x_s}\right)_{P,T} \tag{A.6}$$

and can be computed from eq A.2 as

$$f_{ss} = x_s \frac{\partial \ln f_s}{\partial x_s} \tag{A.7}$$

i.e.

$$f_{ss} = \frac{dx_s}{2M_w(x_s - 1)^2} + 2a\beta(x_s - 1)x_s - 6b\beta$$
$$x_s(1 - 3x_s + 2x_s^2)$$
$$+ \frac{c\sqrt{b^\circ}x_s}{M_w(x_s - 1)^2\sqrt{\frac{x_s}{2M_w(1 - x_s)}}\left(2\sqrt{b^\circ} + \sqrt{2}\sqrt{\frac{x_s}{M_w(1 - x_s)}}\right)^2} \tag{A.8}$$

■ ASSOCIATED CONTENT

Ⓢ Supporting Information

Details on the simulation settings, the fitting coefficients of the function given by eq A.2, as well as figures illustrating the time evolution of structural parameters characterizing the lipid bilayer and protein simulations are provided. This material is available free of charge via the Internet at http://pubs.acs.org.

■ AUTHOR INFORMATION

Corresponding Author

*Phone: +43 1 476548302. Fax: + 43 1 476548309. E-mail: chris.oostenbrink@boku.ac.at.

Notes

The authors declare no competing financial interest.

■ REFERENCES

(1) Karplus, M.; McCammon, J. A. *Nat. Struct. Biol.* **2002**, *9*, 646−652.

(2) Norberg, J.; Nilsson, L. *Q. Rev. Biophys.* **2003**, *36*, 257−306.

(3) van Gunsteren, W. F.; Bakowies, D.; Baron, R.; Chandrasekhar, I.; Christen, M.; Daura, X.; Gee, P.; Geerke, D. P.; Glättli, A.; Hünenberger, P. H.; Kastenholz, M. A.; Oostenbrink, C.; Schenk, M.; Trzesniak, D.; van der Vegt, N. F. A.; Yu, H. B. *Angew. Chem., Int. Ed.* **2006**, *45*, 4064−4092.

(4) Hünenberger, P. H.; van Gunsteren, W. F. Empirical classical force fields for molecular systems. In *Lecture Notes in Chemistry*; Sax, A. F., Ed.; Springer Verlag: Berlin, Germany, 1999; pp 177−214.

(5) MacKerell, D. A., Jr. *J. Comput. Chem.* **2004**, *25*, 1584−1604.

(6) Berendsen, H. J. C. *Simulating the Physical World*; Cambridge University Press: Cambridge, U.K., 2007.

(7) Lii, J.-H.; Allinger, N. L. *J. Am. Chem. Soc.* **1989**, *111*, 8576−8582.

(8) Rappe, A. K.; Casewit, C. J.; Colwell, K. S.; Goddard, W. A.; Skiff, W. M. *J. Am. Chem. Soc.* **1992**, *114*, 10024−10035.

(9) Engelsen, S. B.; Fabricius, J.; Rasmussen, K. *Acta Chem. Scand.* **1994**, *48*, 553−565.

(10) Hwang, M.-J.; Stockfisch, T. P.; Hagler, A. T. *J. Am. Chem. Soc.* **1994**, *116*, 2515−2525.

(11) Hagler, A. T.; Ewig, C. S. *Comput. Phys. Commun.* **1994**, *84*, 131−155.

(12) Halgren, T. A. *J. Comput. Chem.* **1996**, *17*, 616−641.

(13) Gaedt, K.; Holtje, H. D. *J. Comput. Chem.* **1998**, *19*, 935−946.

(14) MacKerell, A. D., Jr.; Bashford, D.; Bellott, M.; Dunbrack, R. L.; Evanseck, J. D.; Field, M. J.; Fischer, S.; Gao, J.; Guo, H.; Ha, S.; Joseph-McCarthy, D.; Kuchnir, L.; Kuczera, K.; Lau, F. T. K.; Mattos, C.; Michnick, S.; Ngo, T.; Nguyen, D. T.; Prodhom, B.; Reiher, W. E.; Roux, B.; Schlenkrich, M.; Smith, J. C.; Stote, R.; Straub, J.; Watanabe, M.; Wiorkiewicz-Kuczera, J.; Yin, D.; Karplus, M. *J. Phys. Chem. B* **1998**, *102*, 3586−3616.

(15) Hatcher, E. R.; Guvench, O.; MacKerell, A. D., Jr. *J. Chem. Theory Comput.* **2009**, *5*, 1315−1327.

(16) Pearlman, D. A.; Case, D. A.; Caldwell, J. D.; Ross, W. S.; Cheatham, T. E., III; DeBolt, S.; Fergusson, D.; Seibel, G.; Kollman, P. *Comput. Phys. Commun.* **1995**, *91*, 1−41.

(17) Cornell, W. D.; Cieplak, P.; Bayly, C. I.; Gould, I. R.; Merz, K. M.; Ferguson, D. M.; Spellmeyer, D. C.; Fox, T.; Caldwell, J. W.; Kollman, P. A. *J. Am. Chem. Soc.* **1995**, *117*, 5179−5197.

(18) Kirschner, K. N.; Yongye, A. B.; Tschampel, S. M.; Gonzalez-Outerino, J.; Daniels, C. R.; Foley, B. L.; Woods, R. J. *J. Comput. Chem.* **2008**, *29*, 622−655.

(19) Kaminski, G. A.; Friesner, R. A.; Tirado-Rives, J.; Jorgensen, W. L. *J. Phys. Chem. B* **2001**, *105*, 6474−6487.

(20) Horta, B. A. C.; Fuchs, P. F. J.; van Gunsteren, W. F.; Hünenberger, P. H. *J. Chem. Theory Comput.* **2011**, *7*, 1016−1031.

(21) Schmid, N.; Eichenberger, A. P.; Choutko, A.; Riniker, S.; Winger, M.; Mark, A. E.; van Gunsteren, W. F. *Eur. Biophys. J.* **2011**, *40*, 843−856.

(22) Reif, M. M.; Hünenberger, P. H.; Oostenbrink, C. *J. Chem. Theory Comput.* **2012**, *8*, 3705−3723.

(23) Berendsen, H. J. C.; Postma, J. P. M.; van Gunsteren, W. F.; Hermans, J. Interaction models for water in relation to protein hydration. In *Intermolecular Forces*; Pullman, B., Ed.; Reidel: Dordrecht, The Netherlands, 1981; pp 331−342.

(24) Oostenbrink, C.; Villa, A.; Mark, A. E.; van Gunsteren, W. F. *J. Comput. Chem.* **2004**, *25*, 1656−1676.

(25) Hünenberger, P. H.; Reif, M. M. *Single−ion Solvation: Experimental and Theoretical Approaches to Elusive Thermodynamic Quantities*, 1st ed.; Royal Society of Chemistry (Theoretical and Computational Chemistry Series): London, UK, 2011; ISBN: 978-1-84755-187-0.

(26) Lins, R. D.; Hünenberger, P. H. *J. Comput. Chem.* **2005**, *26*, 1400−1412.

(27) Soares, T. A.; Hünenberger, P. H.; Kastenholz, M. A.; Kräutler, V.; Lenz, T.; Lins, R. D.; Oostenbrink, C.; van Gunsteren, W. F. *J. Comput. Chem.* **2005**, *26*, 725−737.

(28) Poger, D.; van Gunsteren, W. F.; Mark, A. E. *J. Comput. Chem.* **2009**, *31*, 1117−1125.

(29) Chiu, S.-W.; Clark, M.; Balaji, V.; Subramaniam, S.; Scott, H. J.; Jakobsson, E. *Biophys. J.* **1995**, *69*, 1230−1245.

(30) Reif, M. M.; Hünenberger, P. H. *J. Chem. Phys.* **2011**, *134*, 144104/1−144104/25.

(31) Kukol, A. *J. Chem. Theory Comput.* **2009**, *5*, 615−626.

(32) Autieri, E.; Sega, M.; Pederiva, F.; Guella, G. *J. Chem. Phys.* **2010**, *133*, 095104/1−095104/14.

(33) Hansen, H. S.; Hünenberger, P. H. *J. Comput. Chem.* **2011**, *32*, 998−1032.

(34) Pol-Fachin, L.; Rusu, V. H.; Verli, H.; Lins, R. D. *J. Chem. Theory Comput.* **2012**, *8*, 4681−4690.

(35) van Gunsteren, W. F.; Billeter, S. R.; Eising, A. A.; Hünenberger, P. H.; Krüger, P.; Mark, A. E.; Scott, W. R. P.; Tironi, I. G. *Biomolecular Simulation: The GROMOS96 Manual and User Guide*; Verlag der Fachvereine: Zürich, Switzerland, 1996.

(36) Slater, J. C.; Kirkwood, J. G. *Phys. Rev.* **1931**, *37*, 682−697.

(37) Baldwin, R. L. *Biophys. J.* **1996**, *71*, 2056−2063.

(38) Kunz, W.; Henle, J.; Ninham, B. W. *Curr. Opin. Chem. Biol.* **2004**, *10*, 658−663.

(39) Zhang, Y.; Cremer, P. S. *Curr. Opin. Chem. Biol.* **2006**, *10*, 658−663.

(40) Collins, K. D.; Neilson, G. W.; Enderby, J. E. *Biophys. Chem.* **2007**, *128*, 95−104.

(41) Reif, M. M.; Kräutler, V.; Kastenholz, M. A.; Daura, X.; Hünenberger, P. H. *J. Phys. Chem. B* **2009**, *113*, 3112−3128.

(42) Weerasinghe, S.; Smith, P. E. *J. Chem. Phys.* **2003**, *119*, 11342−11349.

(43) Dill, K. A. *Biochemistry* **1990**, *29*, 7133−7155.

(44) Kumar, S.; Nussinov, R. *J. Mol. Biol.* **1999**, *293*, 1241−1255.

(45) Takano, K.; Tsuchimori, K.; Yamagata, Y.; Yutani, K. *Biochemistry* **2000**, *39*, 12375−12381.

(46) Strop, P.; Mayo, S. L. *Biochemistry* **2000**, *39*, 1251−1255.

(47) Vlachy, N.; Jagoda-Cwiklik, B.; Vácha, R.; Touraud, D.; Jungwirth, P.; Kunz, W. *Adv. Colloid Interface Sci.* **2008**, *146*, 42−47.

(48) Hess, B.; van der Vegt, N. F. A. *Proc. Natl. Acad. Sci. U. S. A.* **2009**, *106*, 13296−13300.

(49) Schmid, N.; Christ, C. D.; Christen, M.; Eichenberger, A. P.; van Gunsteren, W. F. *Comput. Phys. Commun.* **2012**, *183*, 890−903.

(50) Glättli, A.; Daura, X.; van Gunsteren, W. F. *J. Chem. Phys.* **2002**, *116*, 9811−9828.

(51) Malde, A. K.; Zuo, L.; Breeze, M.; Stroet, M.; Poger, D.; Nair, P. C.; Oostenbrink, C.; Mark, A. E. *J. Chem. Theory Comput.* **2011**, *7*, 4026−4037.

(52) Nagle, J. F.; Zhang, R.; Tristram-Nagle, S.; Sun, W.; Petrache, H. I.; Suter, R. M. *Biophys. J.* **1996**, *70*, 1419−1431.

(53) Kučerka, N.; Nagle, J. F.; Sachs, J. N.; Feller, S. E.; Pencer, J.; Jackson, A.; Katsaras, J. *Biophys. J.* **2008**, *95*, 2356−2367.

(54) Nagle, J. F.; Tristram−Nagle, S. *Biochim. Biophys. Acta* **2000**, *1469*, 159−195.

(55) Kučerka, N.; Tristram-Nagle, S.; Nagle, J. F. *Biophys. J.* **2006**, *90*, L83−L85.

(56) Artemyiuk, P. J.; Blake, C. C. F.; Rice, D. W.; Wilson, K. S. *Acta Crystallogr., Sect. B* **1982**, *38*, 778−783.

(57) Auweter, S. D.; Fasan, R.; Reymond, L.; Underwood, J. G.; Black, D. L.; Pitsch, S.; Allain, F. H.-T. *EMBO J.* **2006**, *25*, 163−173.

(58) Ökvist, M.; Dey, R.; Sasso, S.; Grahn, E.; Kast, P.; Krengel, U. *J. Mol. Biol.* **2006**, *357*, 1483−1499.

(59) Steinmetz, M. O.; Jelesarov, I.; Matousek, W. M.; Honnappa, S.; Jahnke, W.; Missimer, J. H.; Frank, S.; Alexandrescu, A. T.; Kammerer, R. A. *Proc. Natl. Acad. Sci. U. S. A.* **2007**, *104*, 7062−7067.

(60) Schindelin, H.; Jiang, W.; Inouye, M.; Heinemann, U. *Proc. Natl. Acad. Sci. U. S. A.* **1994**, *91*, 5119−5123.

(61) Gallagher, T.; Alexander, P.; Bryan, P.; Gilliland, G. L. *Biochemistry* **1994**, *33*, 4721−4729.

(62) Edmondson, S. P.; Qiu, L.; Shriver, J. W. *Biochemistry* **1995**, *34*, 13289−13304.

(63) Schmid, N.; Zagrovic, B.; van Gunsteren, W. F. *Biochemistry* **2007**, *46*, 6500−6512.

(64) Hockney, R. W. *Methods Comput. Phys.* **1970**, *9*, 136−211.

(65) Ryckaert, J.-P.; Ciccotti, G.; Berendsen, H. J. C. *J. Comput. Phys.* **1977**, *23*, 327−341.

(66) Berendsen, H. J. C.; Postma, J. P. M.; van Gunsteren, W. F.; di Nola, A.; Haak, J. R. *J. Chem. Phys.* **1984**, *81*, 3684−3690.

(67) Mie, G. *Ann. Phys.* **1903**, *316*, 657−697.

(68) Jones, J. E. *Proc. R. Soc. London, Ser. A* **1924**, *106*, 441−462.

(69) Jones, J. E. *Proc. R. Soc. London, Ser. A* **1924**, *106*, 463−477.

(70) Barker, J. A.; Watts, R. O. *Mol. Phys.* **1973**, *26*, 789−792.

(71) Berendsen, H. J. C.; van Gunsteren, W. F.; Zwinderman, H. R. J.; Geurtsen, R. G. *Ann. N.Y. Acad. Sci.* **1986**, *482*, 269−285.

(72) Heinz, T. N.; van Gunsteren, W. F.; Hünenberger, P. H. *J. Chem. Phys.* **2001**, *115*, 1125−1136.

(73) Redlack, A.; Grindlay, J. *Can. J. Phys.* **1972**, *50*, 2815−2825.

(74) de Leeuw, S. W.; Perram, J. W.; Smith, E. R. *Proc. R. Soc. London, Ser. A* **1980**, *373*, 27−56.

(75) Hünenberger, P. H. Lattice−sum methods for computing electrostatic interactions in molecular simulations. In: *Simulation and theory of electrostatic interactions in solution: Computational chemistry, biophysics, and aqueous solution.*; Hummer, G., Pratt, L. R., Eds.; American Institute of Physics: New York, 1999; pp 17−83.

(76) Hockney, R. W.; Eastwood, J. W. *Computer Simulation Using Particles*; McGraw-Hill: New York, 1981.

(77) Luty, B. A.; Tironi, I. G.; van Gunsteren, W. F. *J. Chem. Phys.* **1995**, *103*, 3014−3021.

(78) Hünenberger, P. H. *J. Chem. Phys.* **2000**, *113*, 10464−10476.

(79) Robinson, R. A.; Stokes, R. H. *Electrolyte Solutions*, 2nd ed.; Butterworths: London, UK, 1970.

(80) Kirkwood, J. G.; Buff, F. P. *J. Chem. Phys.* **1951**, *19*, 774−777.

(81) Ben-Naim, A. *Statistical Thermodynamics for Chemists and Biochemists*, 1st ed.; Plenum Press: New York, 1992.

(82) Ben-Naim, A. *Molecular Theory of Solutions.*; Oxford University Press: Oxford, UK, 2006.

(83) Schnell, S. K.; Liu, X.; Simon, J.-M.; Bardow, A.; Bedeaux, D.; Vlugt, T. J. H.; Kjelstrup, S. *J. Phys. Chem. B* **2011**, *115*, 10911−10918.

(84) Schnell, S. K.; Vlugt, T. J. H.; Simon, J.-M.; Bedeaux, D.; Kjelstrup, S. *Chem. Phys. Lett.* **2011**, *504*, 199−201.

(85) Friedman, H. L.; Ramanathan, P. S. *J. Phys. Chem.* **1970**, *74*, 3756−3765.

(86) Chitra, R.; Smith, P. E. *J. Phys. Chem. B* **2002**, *106*, 1491−1500.

(87) Kabsch, W.; Sander, C. *Biopolymers* **1983**, *22*, 2577−2637.

(88) Schwalbe, H.; Grimshaw, S. B.; Spencer, A.; Buck, M.; Boyd, J.; Dobson, C. M.; Redfield, C.; Smith, L. J. *Protein Sci.* **2001**, *10*, 677−688.

(89) Dolenc, J.; Missimer, J. H.; Steinmetz, M. O.; van Gunsteren, W. F. *J. Biomol. NMR* **2010**, *47*, 221−235.

(90) Wuthrich, K.; Billeter, M.; Braun, W. *J. Mol. Biol.* **1983**, *169*, 949−961.

(91) Fletcher, C. M.; Jones, D. N. M.; Diamond, R.; Neuhaus, D. *J. Biomol. NMR* **1996**, *8*, 292−310.

(92) Karplus, M. *J. Chem. Phys.* **1959**, *30*, 11−15.

(93) Pardi, A.; Billeter, M.; Wüthrich, K. *J. Mol. Biol.* **1984**, *180*, 741−751.

(94) Eichenberger, A. P.; Allison, J. R.; Dolenc, J.; Geerke, D. P.; Horta, B. A. C.; Meier, K.; Oostenbrink, C.; Schmid, N.; Steiner, D.; Wang, D.; van Gunsteren, W. F. *J. Chem. Theory Comput.* **2011**, *7*, 3379−3390.

(95) Kastenholz, M. A.; Hünenberger, P. H. *J. Chem. Phys.* **2006**, *124*, 124106/1−124106/27.

(96) Hess, B.; Holm, C.; van der Vegt, N. F. A. *J. Chem. Phys.* **2006**, *124*, 164509/1−164509/8.

(97) Anézo, C.; de Vries, A. H.; Höltje, H.−D.; Tieleman, D. P.; Marrink, S.-J. *J. Phys. Chem. B* **2003**, *107*, 9424−9433.

(98) de Bakker, P. I. W.; Hünenberger, P. H.; McCammon, J. A. *J. Mol. Biol.* **1999**, *285*, 1811−1830.

(99) Peter, C.; van Gunsteren, W. F.; Hünenberger, P. H. *J. Chem. Phys.* **2003**, *119*, 12205−12223.

(100) Bergdorf, M.; Peter, C.; Hünenberger, P. H. *J. Chem. Phys.* **2003**, *119*, 9129−9144.

(101) Bonner, O. D. *J. Chem. Soc., Faraday Trans. 1* **1981**, *77*, 2515−2518.

(102) Macaskill, J. B.; Robinson, R. A.; Bates, R. G. *J. Chem. Eng. Data* **1977**, *22*, 411−412.

(103) Lis, L. J.; McAlister, M.; Fuller, N.; Rand, R. P.; Parsegian, V. A. *Biophys. J.* **1982**, *37*, 657−665.

(104) Redlich, O.; Kister, A. T. *J. Am. Chem. Soc.* **1949**, *71*, 505−507.

(105) Guggenheim, E. A. *Philos. Mag.* **1935**, *19*, 588−643.